

Minute-cadence Observations of the LAMOST Fields with the TMTS: VI. Absolute Physical Parameters of Contact Binaries

QIQI XIA,¹ XIAOFENG WANG,^{1,*} KAI LI,² XIANG GAO,² FANGZHOU GUO,¹ JIE LIN,^{3,4} CHENG LIU,⁵ JUN MO,¹ HAOWEI PENG,¹ QICHUN LIU,¹ GAOBO XI,¹ SHENGYU YAN,¹ XIAOJUN JIANG,⁶ JICHENG ZHANG,⁷ CUI-YING SONG,¹ JIANRONG SHI,⁶ XIAORAN MA,¹ DANFENG XIANG,^{1,5} AND WENXIONG LI⁶

¹*Physics Department and Tsinghua Center for Astrophysics, Tsinghua University, Beijing, 100084, People's Republic of China*

²*Shandong Key Laboratory of Optical Astronomy and Solar-Terrestrial Environment, School of Space Science and Physics, Institute of Space Sciences, Shandong University, Weihai, Shandong 264209, China*

³*Department of Astronomy, University of Science and Technology of China, Hefei 230026, People's Republic of China*

⁴*School of Astronomy and Space Science, University of Science and Technology of China, Hefei 230026, People's Republic of China*

⁵*Beijing Planetarium, Beijing Academy of Sciences and Technology, Beijing, 100044, People's Republic of China*

⁶*National Astronomical Observatories, Chinese Academy of Sciences, Beijing 100101, China*

⁷*School of Physics and Astronomy, Beijing Normal University, Beijing 100875, China.*

ABSTRACT

With the development of wide-field surveys, a large amount of data on short-period W UMa contact binaries have been obtained. Continuous and uninterrupted light curves as well as high-resolution spectroscopic data are crucial in determining the absolute physical parameters. Targets with both TMTS light curves and LAMOST medium-resolution spectra were selected. The absolute physical parameters were inferred with the W-D code for ten systems, all of them are W-type shallow or medium contact binaries. The O'Connell effect observed in the light curves can be explained by adding a spot on the primary or secondary component in the models. According to O-C analysis, the orbital periods exhibit a long-term increasing or decreasing trend, amongst which J0132, J1300, and J1402 show periodic variations that may be attributed to the presence of a third body or magnetic activity cycles. Spectral subtraction analysis revealed that the equivalent width of H α indicates strong magnetic activity in J0047, J0305, J0638, and J1402. Among the 10 selected binary systems, except for J0132 and J0913, the more massive components are found to be main-sequence stars while the less massive components have evolved off the main sequence. In J0132, both components are in the main sequence, whereas both components of J0913 lie above the terminal-age main sequence. Based on the relationship between orbital angular momentum and total mass for these two systems, as well as their low fill-out factors, it is possible that these two systems are newly formed contact binaries, having recently evolved from the detached configuration.

1. INTRODUCTION

W Ursae Majoris (W UMa) type contact binaries are a class of eclipsing binary stars where both components share a common envelope and are in contact with each other (Lucy 1968a,b). These systems are characterized by their short orbital periods, typically less than a day, and nearly identical spectral types (late type) for two components. Binnendijk (1970) classified W UMa type contact binaries into two types: W-type and A-type. In W-type systems, the more massive component is cooler than the less massive one, while in A-type systems, the more massive component is hotter (Yildiz & Doğan 2013; Li et al. 2021b). The continuous exchange of mass and energy between the two stars leads to complex evolutionary processes, for example, the thermal relaxation oscillation theory (Flannery 1976; Lucy 1976; Robertson & Eggleton 1977; Lucy & Wilson 1979; Qian 2001), the O'Connell effect (O'Connell 1951), and long-term increase or decrease in the orbital period (Li et al. 2015; Li 2018; Lee & Park 2018).

Radial velocity (RV) measurements play a critical role in the precise determination of the absolute physical parameters of the contact binaries (e.g., Hrivnak 1988, 1989; Rucinski et al. 2000), which requires multiple short exposure-time spectra with high signal-to-noise ratios (SNR). Precise parameters for masses, radii, and luminosities were determined

* E-mail: wang_xf@mail.tsinghua.edu.cn

by combining radial velocities with light curves (e.g., Lu et al. 2007; Alvarez et al. 2015; Liu et al. 2023a). These factors are crucial for explaining the formation and evolution of contact binaries as well as for the mechanisms of mass transfer, angular momentum loss, and the overall stability of the common envelope. Latković et al. (2021) compiled 700 contact binaries from individual studies, among which the absolute physical parameters of 159 targets were determined by spectroscopic and photometric observations. Li et al. (2021b) compiled the absolute physical parameters of 173 contact binaries with spectroscopic and photometric observations.

In recent years, with the release of large-scale photometric and spectroscopic survey data, e.g., the All Sky Automated Survey (ASAS; Pojmanski 1997, 1998, 2002), the All-Sky Automated Survey for Supernovae (ASAS-SN; Shappee et al. 2014; Christy et al. 2023), the Catalina Sky Survey (CSS; Marsh et al. (2017)), the Super Wide Angle Search for Planets (SuperWASP; Pollacco et al. 2006), the Transiting Exoplanet Survey Satellite (TESS; Ricker et al. 2010; Stassun et al. 2018), the Zwicky Transient Facility, (ZTF; Masci et al. 2019; Bellm et al. 2019), and the Large Sky Area Multi-Object Fiber Spectroscopic Telescope (LAMOST; Cui et al. 2012; Zhao et al. 2012), a batch of physical parameters of contact binaries have been obtained. Wilson-Devinney (W-D) program (Wilson & Devinney 1971; Wilson 1979, 1990; Van Hamme & Wilson 2007; Wilson et al. 2010; Wilson & Van Hamme 2014) and PHysics Of Eclipsing BinariEs (PHOEBE) Python code (Prša 2018) are the most commonly used tools to individually solve the orbital parameters of contact binaries (e.g., Deb & Singh 2011; Sun et al. 2020a; Paki & Poro 2024). In addition, methods that use machine learning to solve a large number of orbital parameters simultaneously are also being widely developed (e.g., Ding et al. 2021, 2023; Xiong et al. 2024; Li et al. 2024b), which has greatly facilitated the study of W UMa binaries.

Continuous, uninterrupted light curves and high-precision radial velocity measurements enable accurate determinations of the absolute physical parameters of these systems, allowing for more detailed investigations of the interactions and evolutionary processes within W UMa systems. The Tsinghua University–Ma Huateng Telescopes for Survey (TMTS) have been continuously monitoring the LAMOST sky areas for the white-light band (TMTS *L* band covers a wavelength range from 400 to 900 nm) with uninterrupted observation throughout the night (Zhang et al. 2020b). During the first two years of observation, TMTS has detected a series of variable stars with periods shorter than 7.5 hours (Lin et al. 2022). A total of 1,100 targets with periods shorter than 2 hours were confirmed (Lin et al. 2023a), which includes a blue large-amplitude pulsator (BLAP) with a pulsation period of only 18.9 min (Lin et al. 2023b). A theoretical prediction of the hot subdwarf binary of the shortest orbital period was also discovered by TMTS Lin et al. (2024). Additionally, using machine learning, 11,638 variable stars were classified, including 5,698 EW-type eclipsing binaries (Guo et al. 2024, hereafter TMTS-V), which are also the data used in this paper.

This paper aims to address the absolute physical parameters derived for the W UMa type contact binaries from the TMTS-V. By analyzing photometric and spectroscopic data, we seek to elucidate the intricate dynamics and evolutionary pathways of W UMa type binaries. The results of this study will contribute to an understanding of the evolution of close binary stars and the physical processes that govern their behaviors. The data sources and the method are described in Section 2. Sections 3 and 4 introduce O-C (observed minus calculated) analysis and independent investigation of photometry and spectroscopy. The evolutionary state and statistical characteristics are discussed in Section 5. Section 6 provides a brief summary.

2. DATA AND METHOD

2.1. Target Selection

The Tsinghua University–Ma Huateng Telescopes for Survey (TMTS) is located at the Xinglong Station of the National Astronomical Observatory of China (NAOC), using a multitube telescope system consisting of four 40 cm optical telescopes and a large field of view (FoV) of approximately 18 deg² (Zhang et al. 2020b). Luminous filter (L-band hereafter) was conducted a wide wavelength range from 390nm to about 900nm (Zhang et al. 2020b), similar to *Gaia* G band (330-1050nm; Gaia Collaboration et al. 2018). During the first two-year survey, TMTS has monitored 449 LAMOST/TMTS plates by the end of 2022. Machine learning classification was performed on the periodic variable sources obtained from uninterrupted light curves, confirming 5698 W UMa type contact binaries, namely EW contact binaries (Guo et al. 2024).

The Large Sky Area Multi-Object Fiber Spectroscopic Telescope (LAMOST) is a 4 meter Schmidt telescope with a FOV of 5 square degrees, and is equipped with 4,000 fibers (Cui et al. 2012; Luo et al. 2015; Zhao et al. 2012). LAMOST medium resolution survey (MRS) Data Release (DR) 10¹ were used as the source of radial velocities (RVs)

¹ <https://www.lamost.org/dr10/v1.0/>

Table 1. Photometric observation information of the ten targets

Source I.D.	Name	R.A.	Dec.	Obs. Date	P_{TMTS}	P_{VSX}	L_0	G_{abs}	$B_P - R_P$	N_{LRS}	N_{MRS}	VSX type
		degree	degree		day	day	mag	mag	mag			
TMTS J00474579+3931052	J0047	11.941	39.518	Oct. 6, 2022	0.26099	0.26108	14.401	5.468	1.107	2	3	EW ^a
TMTS J01322049+5512196	J0132	23.085	55.205	Oct. 29, 2020	0.40898	0.40094	13.577	3.550	0.680	0	15	EW/KW ^b
TMTS J03050520+2934439	J0305	46.272	29.579	Dec. 16, 2020	0.24118	0.24698	11.804	5.922	1.181	3	6	EW
TMTS J06380824+4412135	J0638	99.534	44.204	Dec. 31, 2021	0.34706	0.35439	13.273	4.452	0.899	1	22	EW
TMTS J07592990+4019452	J0759	119.875	40.329	Jan. 15, 2020	0.28611	0.29595	12.922	4.357	0.788	1	7	EW
TMTS J09135321+4354212	J0913	138.472	43.906	Jan. 18, 2020	0.28207	0.27868	14.763	5.347	1.098	0	87	EW
TMTS J10421306+3849120	J1042	160.554	38.820	Jan. 19, 2020	0.32310	0.31604	13.459	4.239	0.758	2	100	EW
TMTS J13001158+3023102	J1300	195.048	30.386	Apr. 7, 2021	0.29509	0.30199	12.142	4.840	0.947	2	3	EW
TMTS J14020545+3402396	J1402	210.523	34.044	Apr. 14, 2021	0.25532	0.26077	11.835	6.103	1.318	2	3	EW
TMTS J22364231+3041479	J2236	339.176	30.697	Sept. 7, 2022	0.33873	0.33574	13.329	4.227	0.846	1	3	EW

NOTE—Source I.D.: TMTS catalogue identifier; Name: identifier of the target in this study; P_{TMTS} : orbital period from TMTS; P_{VSX} : orbital period from VSX; L_0 : median magnitude from TMTS; G_{abs} : absolute magnitude from Gaia; $B_P - R_P$: color index from Gaia; N_{LRS} : exposure times of LAMOST LR spectra; N_{MRS} : exposure times of LAMOST MR spectra; VSX type: VSX variability type.

^aEW represents the W UMa type eclipsing variables from VSX.

^bKW represents contact systems of the W UMa type, with ellipsoidal components of F0-K spectral type.

for the W UMa contact binaries with a resolution of 7,500. For each observed object, two spectra are obtained within a single exposure, which include a blue (B) side spectrum with a wavelength range of 4950 Å to 5350 Å, and a red (R) side spectrum with a wavelength range of 6300 Å to 6800 Å. The blue arm contains more absorption lines than the red arm, allowing us to measure the RVs with a precision up to 1 km s⁻¹ for most stars (Liu et al. 2019).

Firstly, we cross-matched the EW catalog of TMTS with the LAMOST MRS catalog and filtered according to the following criteria:

- 1 Select targets within an angular radius of 3".
- 2 SNRs of B-band spectra greater than 10.
- 3 Number of consecutive exposures greater than or equal to 3.

After the above selection process, we obtained 57 targets that met the criteria. Then, using the period and times of minimum of the TMTS light curves of each target, we calculated the phase corresponding to the observed times for each target. We chose targets with at least three phases between 0.2-0.3 or 0.7-0.8. After that, we visually inspected their light curves (LCs) again, excluding LCs with insufficient SNR and those targets that might be ellipsoidal variables. Finally ten targets were identified from the LAMOST MRS spectra for subsequent RV calculations, which are listed in Table 1. Figure 1 shows the phase-folded light curves of the ten W UMa contact binaries from the TMTS.

2.2. Target Information

We also cross-matched these targets with VSX (Watson et al. 2006), Gaia (Gaia Collaboration et al. 2016, 2018), and the LAMOST low-resolution (LR) spectra. The information obtained is listed in Table 1 and Table 2. Figure 2 shows the LR spectra, which are typical FGK-type spectra and characterized by apparent Balmer absorption lines.

Table 1 provides information on these targets, including their TMTS catalog identifier (Source ID), Name (in our work), right ascension in decimal degrees (R.A.), Declination in decimal degrees (Dec.), observation date (Obs. Date), orbital period from TMTS (P_{TMTS}), orbital period from VSX (P_{VSX}), median magnitude from TMTS (L_0), absolute magnitude derived from Gaia DR2 database (G_{abs}), color index derived from Gaia DR2 database ($B_P - R_P$), exposure times of LAMOST LR spectra (N_{LRS}), exposure times of LAMOST MR spectra (N_{MRS}), and VSX variability type (VSX type). Table 2 lists the spectral information of the ten targets from LAMOST DR10, including Name, Obs. Date, spectral type (Spec.type), effective temperature (T_{eff}), surface gravity ($\log g$), metallicity (Fe/H), Heliocentric radial velocity (RV), and SNR of the g band (SNR_g).

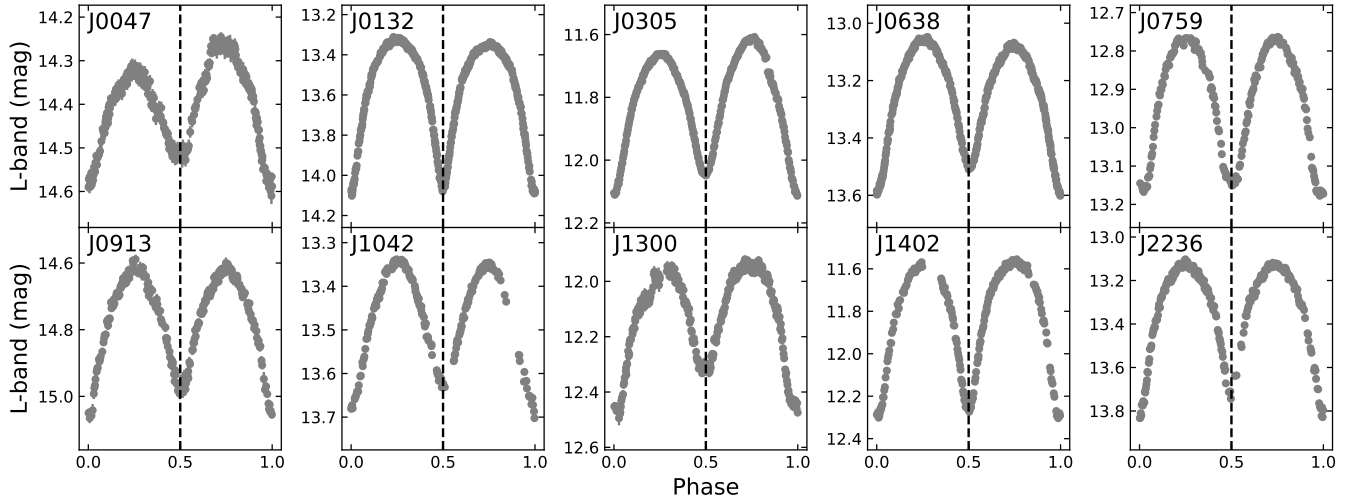


Figure 1. Phase-folded light curves of ten targets from TMTS. The L-band is the TMTS Luminous filter.

All of these targets have been identified as contact binaries or eclipsing binary candidates by the Asteroid Terrestrial-impact Last Alert System (ATLAS) (Heinze et al. 2018) or *Gaia* Data Release 3 (Panchal & Joshi 2021), and their orbital periods have been determined, respectively. The periods, which were used for the phase-folded and orbital period analysis, are listed in Table 5. Among the ten targets, J0132, J0305, J1300 and J1402 have undergone the analysis of multiband photometric solution and studies of period. Detailed explanations of these targets are provided in the following.

(i) J0132 (V471 Cas) was discovered photographically by Hoffmeister (1966), and classified as a W UMa type binary by Gessner & Meinunger (1973). The photometric solution was first applied to J0132 by Liu & Tan (1991), in which the mass ratio was determined as $0.5947(\pm 0.0149)$ and the over-contact factor is 0.19. Kjurkchieva et al. (2019) reanalyzed the new light curves and obtained the mass ratio and fill-out factor with 0.635 and 0.078. Through the analysis of orbital period, they revised the period of J0132 to 0.400937 days and confirmed that J0132 may exist a third body with a sinusoidal period of 12.8 yr.

(ii) J0305 (NSVS 6599082) was first classified as a W UMa type binary by Hoffman et al. (2009). Panchal & Joshi (2021) presented the photometric and spectroscopic analysis, which indicates that J0305 shows a long-term increase in orbital period, with $dp/dt = 1.78(\pm 1.52) \times 10^{-6}$ d yr $^{-1}$. The mass ratio and fill-out factor are $0.31(\pm 0.01)$ and 0.105, respectively, the equivalent width (EW) of H α is measured as 1.031 ± 0.018 Å.

(iii) J1300 (MM Com) was discovered as a contact binary with a period of 0.30199999 days from Robotic Optical Transient Search Experiment (ROTSE) all-sky surveys (Akerlof et al. 2000). Kjurkchieva et al. (2018) obtained light curves in the g' and i' bands and derived the photometric solution. J0913 is a W-type contact binary, with a mass ratio, orbital inclination, and fill-out factor of $4.66(\pm 0.02)$, $80.6^\circ(\pm 0.03)$, and 0.2388, respectively. Then, Yang et al. (2023) analyzed new photometric and spectroscopic data for J1300, determining a mass ratio of $4.747(\pm 0.005)$, an orbital inclination of $79.76^\circ(\pm 0.16)$, and a fill-out factor of $0.32(\pm 0.04)$. The study of O-C suggests that J0913 may be in a triple system with a period of $20.02(\pm 0.43)$ yr.

(iv) J1402 (EI CVn) was discovered as an eclipsing binary system by ROTSE with a period of 0.260775 days (Akerlof et al. 2000). Then it was carried out as a photometric orbital solution by Yang (2011), which was found to be a W-type contact binary with a mass ratio of $0.461(\pm 0.003)$ and a fill-out factor of $0.21(\pm 0.07)$. The $O - C$ analysis indicates that the orbital period of J1402 is decreasing at a long-term rate of $dp/dt = -3.11(\pm 0.03) \times 10^{-7}$ d yr $^{-1}$. Alton & Stepień (2021) obtained the new CCD photometric data of J1402 and performed a W-D analysis, resulting in a mass ratio of $0.443(\pm 0.001)$ and a fill-out factor of 0.15. The study of $O - C$ suggests a long-term period decrease rate of $dp/dt = -1.35(\pm 0.01) \times 10^{-7}$ d yr $^{-1}$, with a periodic modulation of 10.14 ± 1.13 days.

The other six targets, J0047, J0638, J0759, J0913, J1042, and J2236, have not been systematically analyzed since their discovery.

2.3. RV Measurements

Table 2. LAMOST LR spectroscopic observation log of the ten targets.

N	Name	Obs. Date	Spec. type	T_{eff} K	log g dex	Fe/H dex	RV km/s	SNR_g	EW(H α) Å
1	J0047	Dec. 12, 2011	K0	5117.3(\pm 93.8)	4.21(\pm 0.16)	-0.242(\pm 0.101)	12.6(\pm 6.8)	14.9	0.772(\pm 0.091)
		Dec. 9, 2016	G8	5107.9(\pm 22.4)	4.38(\pm 0.03)	-0.158(\pm 0.019)	5.8(\pm 3.0)	51.1	0.917(\pm 0.033)
2	J0132	-	-	-	-	-	-	-	-
3	J0305	Nov. 14, 2014	G9	4915.8(\pm 18.0)	4.45(\pm 0.02)	-0.425(\pm 0.013)	-24.1(\pm 3.0)	150.1	0.916(\pm 0.038)
		Nov. 19, 2014	G9	4838.1(\pm 29.9)	4.36(\pm 0.04)	-0.412(\pm 0.024)	-23.3(\pm 4.2)	93.8	1.086(\pm 0.054)
		Jan. 3, 2015	K4	4719.8(\pm 29.0)	4.41(\pm 0.04)	-0.496(\pm 0.022)	-21.8(\pm 4.6)	133.7	0.951(\pm 0.045)
4	J0638	Mar. 9, 2012	G7	5518.4(\pm 90.6)	4.38(\pm 0.15)	-0.164(\pm 0.098)	26.5(\pm 6.8)	15.7	0.854(\pm 0.100)
5	J0759	Dec. 12, 2014	G8	5143.7(\pm 80.7)	4.69(\pm 0.13)	-0.475(\pm 0.087)	-0.1(\pm 6.0)	15.4	0.085(\pm 0.035)
6	J0913	-	-	-	-	-	-	-	-
7	J1042	Apr. 10, 2013	G0	5551.9(\pm 25.3)	3.90(\pm 0.04)	-0.99 (\pm 0.021)	-6.2(\pm 3.4)	67.6	0.340(\pm 0.032)
		Mar. 3, 2015	F2	5751.5(\pm 17.6)	4.08(\pm 0.03)	-0.834(\pm 0.015)	-7.1(\pm 2.4)	47.0	0.357(\pm 0.044)
8	J1300	Feb. 7, 2015	G7	5455.0(\pm 25.6)	4.13(\pm 0.04)	-0.237(\pm 0.023)	-18.3(\pm 3.5)	41.5	0.357(\pm 0.044)
		May 18, 2016	F9	5548.1(\pm 30.4)	4.17(\pm 0.04)	-0.272(\pm 0.029)	4.0(\pm 3.9)	35.7	0.501(\pm 0.064)
9	J1402	Mar. 25, 2014	K5	4504.5(\pm 34.3)	4.19(\pm 0.05)	0.098(\pm 0.029)	-41.0(\pm 4.6)	59.6	0.823(\pm 0.029)
		Feb. 26, 2018	K5	4582.6(\pm 64.6)	4.33(\pm 0.11)	0.176(\pm 0.069)	-32.2(\pm 4.9)	16.5	0.722(\pm 0.146)
10	J2236	Sept. 19, 2016	G3	5754.1(\pm 27.1)	4.23(\pm 0.04)	-0.193(\pm 0.021)	-27.2(\pm 4.1)	114.6	0.508(\pm 0.024)

In order to obtain the RVs of these ten targets, we first used the Python package *laspec* (Zhang et al. 2020a, 2021) to process the LAMOST MR spectra and measured the cross-correlation functions (CCF) for each component. In this process, PHOENIX (Hauschildt 1993; Hauschildt & Baron 2006; Baron & Hauschildt 2007) was used to construct template spectra, whose resolution was degraded to match that of the LAMOST MR spectra. Simultaneously, since RV zero points (RVZPs) of MR spectra may vary with time and different fibers, we used the method of Zhang et al. (2021) to calibrate RVZPs. Then, to determine the positions of the two peaks of the CCF, we used the Python tool *GaussPy* to fit the RVs of primary and secondary components, which can implement the Autonomous Gaussian Decomposition (AGD) algorithm (Lindner et al. 2015). The RVs obtained for all targets are listed in Table 3.

3. O-C ANALYSIS OF TIMES OF MINIMUM

Since the discovery of these ten targets, orbital period analysis has been conducted only for J0132, J0305, J1300, and J1402, while the other targets remain unanalyzed. Combining the results from some photometric surveys such as ASAS, ASAS-SN, Brno Regional Network of Observers project (BRNO)², CSS, SuperWASP, TESS, and ZTF, we collected as many times of minimum as possible for these ten objects. For survey data spanning long periods, we conducted phase-shifting on them, ensuring that light curves have enough data points within one period. The O-C (observation minus calculation) time span ranges from approximately 5000 to 8500 days, with the folded periods covering data from 8 to 50 days. By dividing the minimum and maximum folded periods of each target by their respective time intervals, we find that the folded periods account for 0.1% to 1% of the entire O-C time interval. The errors resulting from phase shift are acceptable. Times of minimum were calculated using the K-W method (Kwee & van Woerden 1956), which is listed in Table 4. The obtained times of minimum are 209, 195, 253, 136, 38, 22, 175, 243, 231, and 213 for J0047, J0132, J0305, J0638, J0759, J0913, J1042, J1300, J1402, and J2236, respectively.

Then, we calculated their n_c and O-C using the following formula,

$$T = T_0 + P \times n_c, \quad (1)$$

with T_0 and period provided in Table 5. T is the computed moment of the observation. n_c represents the number of cycles. Then O-C was obtained by subtracting the observed times of the minima from the times of the minima calculated using the above formula. Figure 3 shows the relationship between n_c and O-C for each target. All targets exhibit

² <http://var2.astro.cz/EN/brno/index.php>

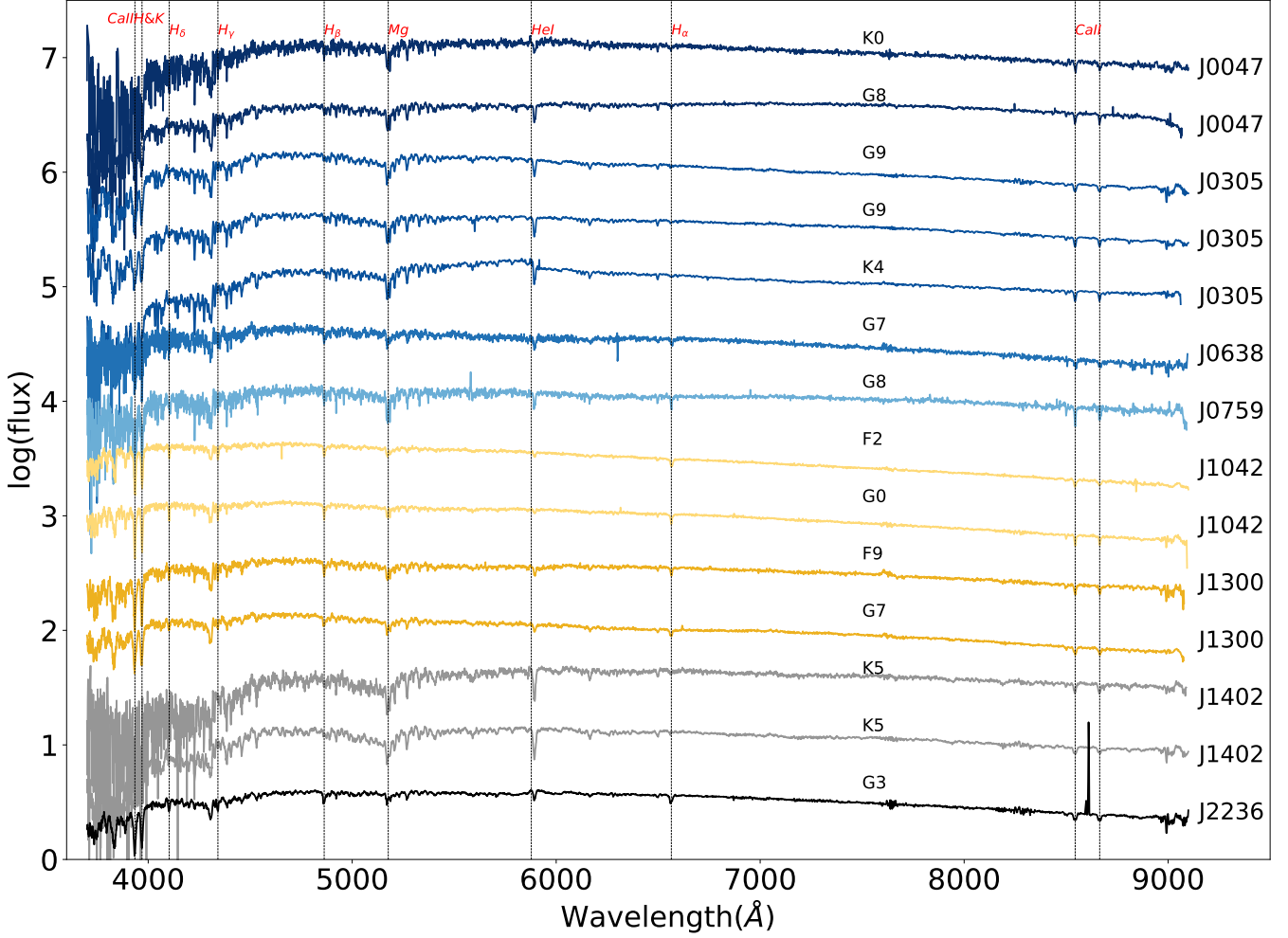


Figure 2. The LAMOST low-resolution spectra of eight targets. The spectral types and positions of some characteristic spectral lines are labeled in the plot. Each spectrum is accompanied by the corresponding name of the target on the right side.

a long-term trend of increasing or decreasing periods. Therefore, we fitted their O-C with a quadratic polynomial. Polynomial coefficients were determined using the least squares method. The corrected epoch, the corrected period and the period change rate (dp/dt) are shown in Table 5. The sign of dp/dt indicates whether the period is increasing (positive) or decreasing (negative) with time.

From the residuals in the bottom panel of each subplot in Figure 3, it can be seen that J0132, J1300 and J1402 exhibit significant periodic variations. This suggests that these systems may have other physical mechanisms, such as magnetic activity cycles or light time travel effect. Then, we fitted their trends of periodic variation using the following formula from Irwin (1952).

$$\begin{aligned}
 (O - C)_1 &= T_0 + \Delta T_0 + (P_0 + \Delta P_0)E + \frac{\beta}{2}E^2 + A[(1 - e^2) \frac{\sin(\nu + \omega)}{(1 + e \cos \nu)}] \\
 &= T_0 + \Delta T_0 + (P_0 + \Delta P_0)E + \frac{\beta}{2}E^2 + A[\sqrt{(1 - e^2)} \sin E^* \cos \omega + \cos E^* \sin \omega - e \sin \omega].
 \end{aligned} \tag{2}$$

T_0 and P_0 represent the initial epoch and initial period, respectively, same as in Equation 1. ΔT_0 and ΔP_0 are used to modify the initial epoch and the period, respectively. β is the long-term change in period, A is the semiamplitude of the cyclic modulation given in days, e is the eccentricity of the supposed third body, ν is the true anomaly, ω is the argument of the periastron in the plane of the orbit, and E^* is the eccentric anomaly (Irwin 1952). According to the fitting, the corresponding fitting curves are shown in Figure 4. The fitting parameters for these three targets are listed in Table 6. The residual panel of each subfigure in Figure 4 shows smooth variations for J0132 and J1402, except for

Table 3. Radial velocities of the ten targets.

JD (Bary.)	Phase	RV ₁	Errors	RV ₂	Errors	JD (Bary.)	Phase	RV ₁	Errors	RV ₂	Errors
2400000+		km s ⁻¹	km s ⁻¹	km s ⁻¹	km s ⁻¹	2400000+		km s ⁻¹	km s ⁻¹	km s ⁻¹	km s ⁻¹
J0047											
59532.09939	0.70922	244.07	1.18	-25.47	0.88	59532.12987	0.76762	250.87	1.80	-34.70	1.10
59532.11463	0.82597	242.28	1.31	-23.66	0.94						
J0132											
58450.02562	0.30095	-236.45	1.52	96.91	1.10	59130.25377	0.86746	128.40	0.91	-145.35	0.85
58450.04197	0.34171	-227.93	1.27	95.11	1.05	59130.23744	0.82673	143.63	0.73	-169.31	0.76
58450.05823	0.38227	-207.58	1.05	77.66	1.04	59130.27005	0.90807	86.75	1.74	-131.80	1.53
J0305											
58410.17413	0.21550	-206.12	1.35	104.86	1.04	58410.20672	0.34747	-180.44	1.37	75.57	1.21
58410.19044	0.28153	-204.74	1.32	99.07	1.06						
J0638											
59544.21399	0.02171	28.63	0.68	319.60	2.35	59562.25380	0.92498	124.04	3.42	-66.83	3.33
59544.22920	0.06462	-43.74	5.14	122.90	5.37	59562.26904	0.96798	135.00	2.51	17.86	4.04
...

NOTE— RV₁ and RV₂ represent the RVs of the primary and secondary stars, respectively. The errors were determined through the CCF procedure for each RV data.

(This table is available in its entirety in machine-readable form.)

Table 4. Times of minimum for the ten targets.

BJD	Error	Method	Ref.	BJD	Error	Method	Ref.	BJD	Error	Method	Ref.
2400000+	(days)			2400000+	(days)			2400000+	(days)		
J0047											
53201.80826	0.00123	CCD	(1)	59859.96397	0.00045	CCD	(2)	59872.75616	0.00036	CCD	(2)
53219.70044	0.00304	CCD	(1)	59860.09476	0.00045	CCD	(2)	59872.88773	0.00039	CCD	(2)
53237.84330	0.00086	CCD	(1)	59860.22457	0.00037	CCD	(2)	59873.01750	0.00051	CCD	(2)
53258.59713	0.00272	CCD	(1)	59860.35601	0.00035	CCD	(2)	59873.14927	0.00034	CCD	(2)
53272.83309	0.00372	CCD	(1)	59860.48686	0.00042	CCD	(2)	59873.27857	0.00038	CCD	(2)

References.(1) superWASP; (2) TESS; (3) TMTS; (4) ZTF; (5) Hubscher (2005); (6) BBSAG124; (7) Dvorak (2005); (8) Hubscher et al. (2005); (9) Hubscher et al. (2006); (10) Nelson (2008); (11) Hubscher et al. (2008); (12) Diethelm (2009a); (13) Diethelm (2010a); (14) Hubscher et al. (2010a); (15) Diethelm (2011a); (16) Hubscher & Lehmann (2012); (17) Diethelm (2012a); (18) JAAVSO; (19) Lampens et al. (2017); (20) Hubscher (2014); (21) Juryšek et al. (2017); (22) Hubscher (2017); (23) ASAS; (24) CSS; (25) Panchal & Joshi (2021); (26) ASAS-SN; (27) ROTSE; (28) BRNO; (29) The o-c gateway; (30) Lewandowski et al. (2007); (31) Nelson (2007); (32) Nelson (2009a); (33) Diethelm (2009b); (34) Hubscher et al. (2010b); (35) Diethelm (2010b); (36) Diethelm (2011b); (37) Hubscher et al. (2012); (38) Hoňková et al. (2013); (39) Diethelm (2012b); (40) Hubscher et al. (2013); (41) Nelson (2013); (42) Honková et al. (2014); (43) Honkova et al. (2015); (44) Yang et al. (2023); (45) Blattler & Diethelm (2003); (46) Diethelm (2005); (47) Diethelm (2006); (48) Diethelm (2007); (49) Nelson (2009b); (50) Yang (2011); (51) Hubscher & Monninger (2011); (52) Demircan et al. (2011); (53) Pagel (2018); (54) Lehký et al. (2021);

(This table is available in its entirety in machine-readable form.)

J1300. The cyclic variation of the O-C for J0132 and J1402 may be due to the light-time effect caused by the presence of a third body. J1300 may be part of a quadruple system. The comprehensive analysis of the orbital period variation will be discussed in Section 5.

4. THE INVESTIGATION OF PHOTOMETRY AND SPECTROSCOPY

Table 5. Ephemerides and period of the ten targets.

Name	T_0 (BJD)	Epoch Ref.	Period days	Period Ref.	Corrected Epoch	Corrected Period days	$\frac{dp}{dt}$ $\times 10^{-8} \text{ d yr}^{-1}$	$\frac{dM_1}{dt}$ $\times 10^{-7} M_\odot \text{ yr}^{-1}$
J0047	2459859.052923	(1)	0.261077	(2)	2459859.050409(± 0.000017)	0.261076(± 0.000001)	-28.84(± 0.01)	0.86(± 0.01)
J0132	2458080.255808	(3)	0.400937	(3)	2458080.255492(± 0.000398)	0.400938(± 0.000001)	6.22(± 0.76)	-1.44(± 0.18)
J0305	2454085.436000	(4)	0.246983	(4)	2454085.459429(± 0.000001)	0.246983(± 0.000001)	7.00(± 0.01)	-0.35(± 0.01)
J0638	2459580.005375	(1)	0.354390	(5)	2459580.005990(± 0.000036)	0.354385(± 0.000001)	-38.03(± 0.07)	7.86(± 0.01)
J0759	2458864.321507	(1)	0.295950	(5)	2458864.323469(± 0.000011)	0.295947(± 0.000001)	25.49(± 0.02)	-0.60(± 0.01)
J0913	2458867.206314	(1)	0.278684	(2)	2458867.207365(± 0.000037)	0.278685(± 0.000001)	41.79(± 0.12)	-25.85(± 0.07)
J1042	2458868.309159	(1)	0.316037	(2)	2458868.310805(± 0.000063)	0.316038(± 0.000001)	-	-
J1300	2451277.840483	(6)	0.301990	(6)	2451277.856993(± 0.001430)	0.301987(± 0.000001)	24.73(± 1.20)	-0.54(± 0.03)
J1402	2454891.208272	(7)	0.260767	(7)	2454891.210399(± 0.000284)	0.260767(± 0.000001)	-21.74(± 0.97)	1.49(± 0.07)
J2236	2459830.048809	(1)	0.335739	(2)	2459830.048690(± 0.000004)	0.335739(± 0.000001)	10.14(± 0.01)	-1.17(± 0.01)

References.(1) TMTS; (2) Heinze et al. (2018); (3) Kjurkchieva et al. (2019); (4) Panchal & Joshi (2021); (5) Sun et al. (2020b); (6) Yang et al. (2023); (7) Yang (2011).

Table 6. The fitted periodic variation parameters of O-C for J0132, J1300 and J1402.

Parameters	J0132	J1300	J1402
A(day)	0.00134 \pm 0.00068	0.00628 \pm 0.00044	0.00382 \pm 0.00040
e	0.752 \pm 0.376	0.857 \pm 0.118	0.619 \pm 0.117
ω (deg)	244.4 \pm 41.0	99.4 \pm 8.6	37.8 \pm 9.6
P_3 (yr)	15.3 \pm 0.5	12.1 \pm 0.2	17.9 \pm 0.5
T_3	2427079 \pm 81664	2444564 \pm 47358	2445689 \pm 63787
$a'_{12} \sin i'$	0.232 \pm 0.066	1.088 \pm 0.076	0.662 \pm 0.069
$f(m)(M_\odot)$	0.00005 \pm 0.00005	0.00880 \pm 0.00185	0.00090 \pm 0.00028
$M_3(M_\odot)$	0.066 \pm 0.032	0.312 \pm 0.041	0.134 \pm 0.025
$a_3(R_\odot)$	9.35 \pm 5.23	6.26 \pm 0.93	8.77 \pm 1.87
Spec. type	-	M3	M5.5
$l_3(L_\odot)$	-	0.016	0.002
l_3/l (%)	-	1.663	0.512
ΔQ_1 (g cm ²)	1.28 $\times 10^{49}$	1.17 $\times 10^{49}$	3.23 $\times 10^{48}$
ΔQ_2 (g cm ²)	1.90 $\times 10^{49}$	5.49 $\times 10^{49}$	5.22 $\times 10^{48}$

4.1. W-D Analysis

We used the 2013 version of the W-D method to analyze the TMTS light curves and the RVs of these ten systems to obtain their orbital and absolute parameters. The initial epoch and period used to convert BJD to phase of each target are the corrected epoch and period in Table 5. During the W-D analysis, we analyzed every light curve with RV for each target simultaneously.

For targets with LAMOST LR spectra, we used the temperature or the average temperature of multiple spectra provided by LAMOST as the effective temperature of the primary star (T_1 , the hotter component) during the W-D process. For targets without LAMOST LR spectra, we examined their LAMOST MR spectra. Since the MR spectra of J0132 did not yield a temperature and the temperature uncertainties for J0913 exceeded 50 K, the temperatures provided by Gaia were adopted as T_1 for these two targets. The specific values T_1 are listed in Table 7. Then we fixed the effective temperature of the primary (T_1) and adjusted that for the secondary (T_2 , the cooler component). The gravity-darkening and bolometric albedo coefficients were set to $g_{1,2} = 0.32$ and $A_{1,2} = 0.5$ following Lucy (1967) and Ruciński (1969). The bolometric limb-darkening and bandpass limb-darkening coefficients were internally computed, which were obtained from van Hamme (1993), and the limb-darkening law is the square root law. The weights of the light curves and the radial velocities were set according to the observation errors, using the reciprocal of the square of the error. During the modeling, the fixed parameters were as follows: the effective temperatures of the primary star T_1 , the orbital period P and the orbital eccentricity e . The orbital eccentricity e was fixed to zero, consistent with the assumption that contact binaries typically have circular orbits due to strong tidal interactions. The adjustable

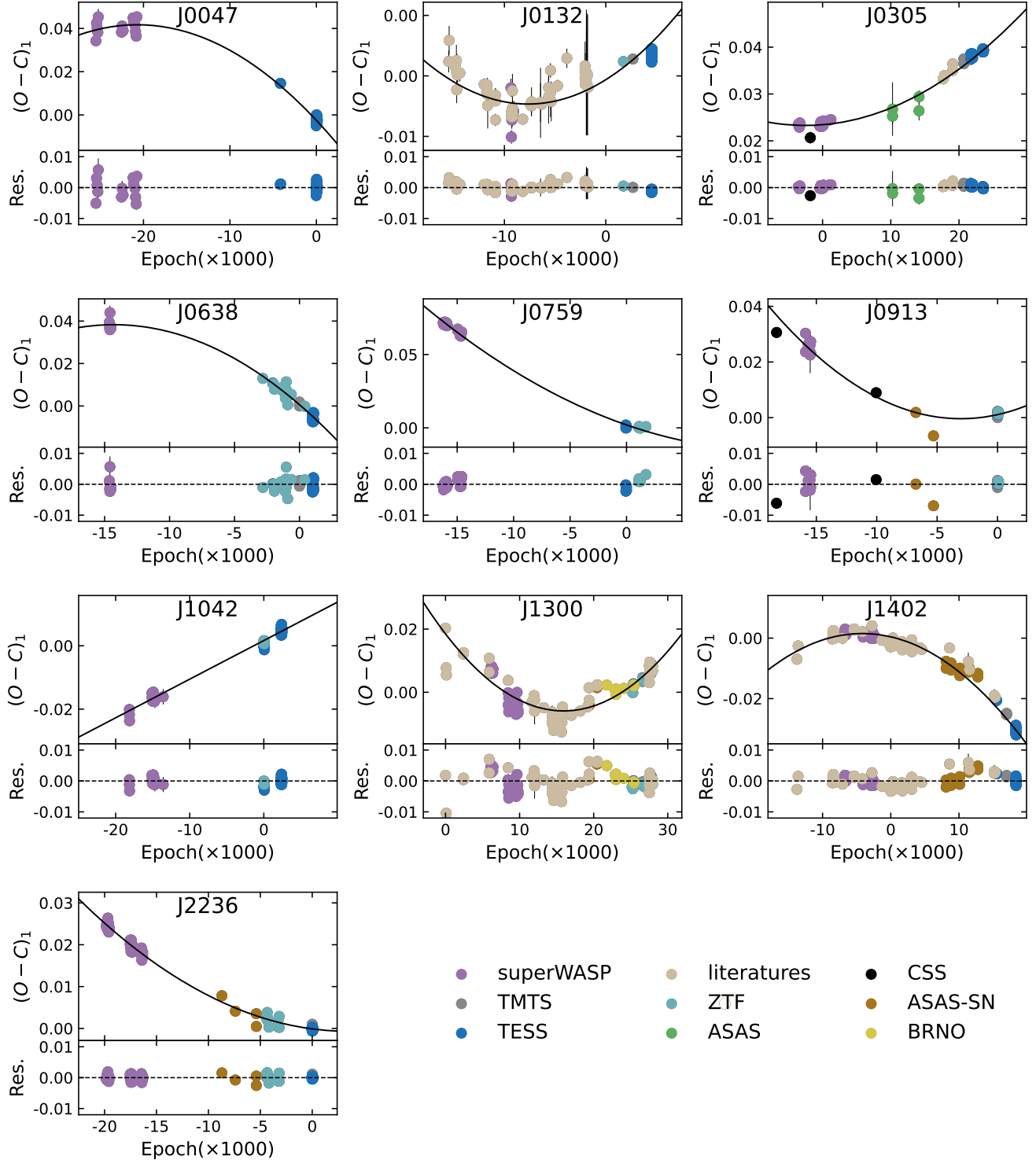


Figure 3. The O-C diagram of the 10 targets presented in this paper. The top panel shows the curve $(O - C)_1$ determined by equation 1. The residuals, which remove the quadratic correction term from the $(O - C)_1$ curve, are plotted in the lower panel. The units of the $(O - C)_1$ and Residual are in days. The errors not given in Table 4 are set to 0.001.

parameters were as follows: the orbital semimajor axis a , the systemic radial velocity V_γ , the orbital inclination i , the mass ratio $q = M_2/M_1$, the effective temperature of the secondary star T_2 , the monochromatic luminosity of the primary star L_1 and the dimensionless potential of the two components $\Omega_1 = \Omega_2$. The fill-out factor was calculated

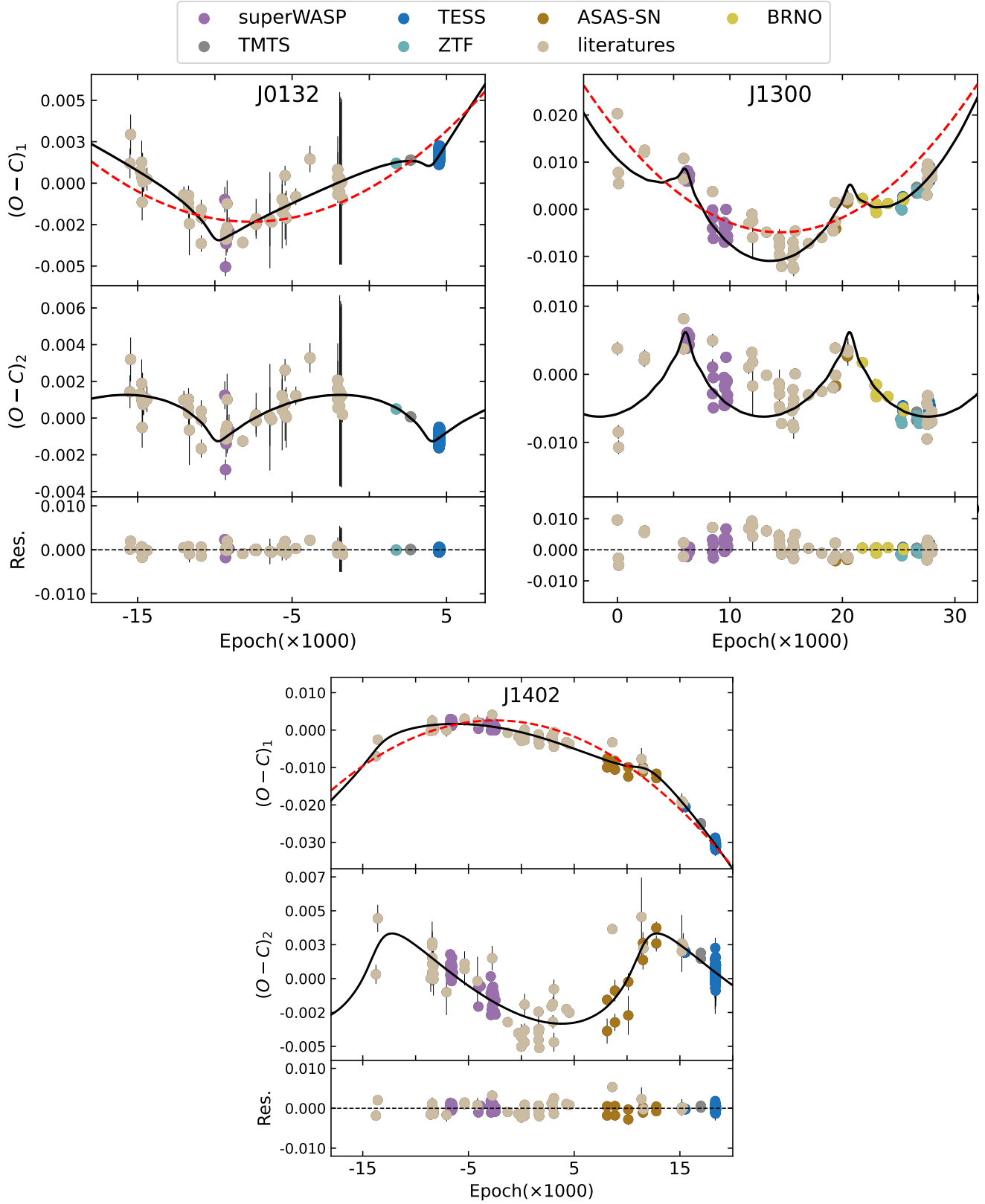


Figure 4. The O-C diagram of J0132, J1300 and J1402 with periodic variations. The top panel shows the $(O - C)_1$ curve determined by Equation 1 as in the top panel of Figure 3. The $(O - C)_2$, which remove the quadratic correction term from the $(O - C)_1$ curve, are plotted in the middle panel. The residuals from the full ephemeris of Equation 3 are displayed in the lower panel. The units of $(O - C)_1$, $(O - C)_2$, and Residual are in days. The different colors of the symbols represent different data, as explained in the diagram.

by $f = (\Omega - \Omega_{in}) / (\Omega_{out} - \Omega_{in})$, where Ω , Ω_{in} and Ω_{out} represent potentials for the common photosphere, the inner and outer contact surfaces, respectively. When $f = 0$, the two components just fill the inner contact surface and begin to contact, when $f = 1$, the two components have already filled the outer contact surface. After running the automatic iteration, the convergence criterion was established as the condition in which the standard error of the adjustable parameters is greater than their respective correction values, and the difference between the input mean residual and the predicted mean residual does not exceed 1%.

From their TMTS light curves, it can be seen that the two maxima at phases 0.25 and 0.75 exhibit some difference, a phenomenon known as the O’Connell effect, which is typically attributed to the magnetic activity of the components (e.g., Guo et al. 2020; Li et al. 2021a; Papageorgiou et al. 2023; Ćeki et al. 2024). Meanwhile, Doppler-boosting also contributes to the observed flux variations (Loeb & Gaudi 2003; Zucker et al. 2007). Therefore, a dark spot or a hot spot model was employed during the W-D analysis to obtain a better fit first. All targets used models with a dark spot added to either the primary or the secondary star. The latitude were both fixed at 90° , because the most reliable parameter of a spot is the longitude of the spot, which can be used to study the evolution of the spot and stellar activity cycles (Eker 1999; Berdyugina 2005). Subsequently, we calculated the observed magnitude variations, Δm ($m_{0.25} - m_{0.75}$), in phases 0.25 and 0.75 from the light curves derived from the W-D fitting and listed in Table 7. For each target, considering the temperatures (T_{eff}) of the components and the observational band ($\lambda \approx 650\text{nm}$), the beaming factors were determined (Zucker et al. 2007). Using the radial velocities of each component at phases 0.25 and 0.75, we calculated the beaming-magnitude variations for each target. All of these values are listed in Table 7. The observed magnitude variations are on the order of percent of a magnitude, while the beaming-magnitude variations are on the order of thousandths. Therefore, Doppler boosting is unlikely to explain the O’Connell effect. The spot model was adopted to account for the O’Connell effect.

The orbital and spot parameters determined by the light curves and the radial velocities are all tabulated in Table 7. The uncertainties of the adjustable parameters are only internal uncertainties of the final step of the light curve analysis determined by W-D code. To account for the uncertainty of T_1 derived from spectroscopy to T_2 , we conducted the following discussion. Based on photometric data, the W-D code can precisely determine T_2/T_1 . Therefore, assuming T_1 is fixed, the uncertainty of T_2 derived from W-D can be used to determine the uncertainty of T_2/T_1 . Subsequently, combining the uncertainties of T_2/T_1 and T_1 , the accurate uncertainty of T_2 can be obtained. The final uncertainties of T_1 and T_2 are also listed in Table 7. Theoretical light curves and radial velocities for the ten targets are shown in Figure 5. The smooth residuals of the light curves indicate that the model with the added spot resulted in a good fit for all ten targets. Figure 6 shows the geometric structures of each target, we can clearly see the location and angular radius of the spots. Table 7 also provides absolute physical parameters from the W-D process, with detailed descriptions presented in Section 5.

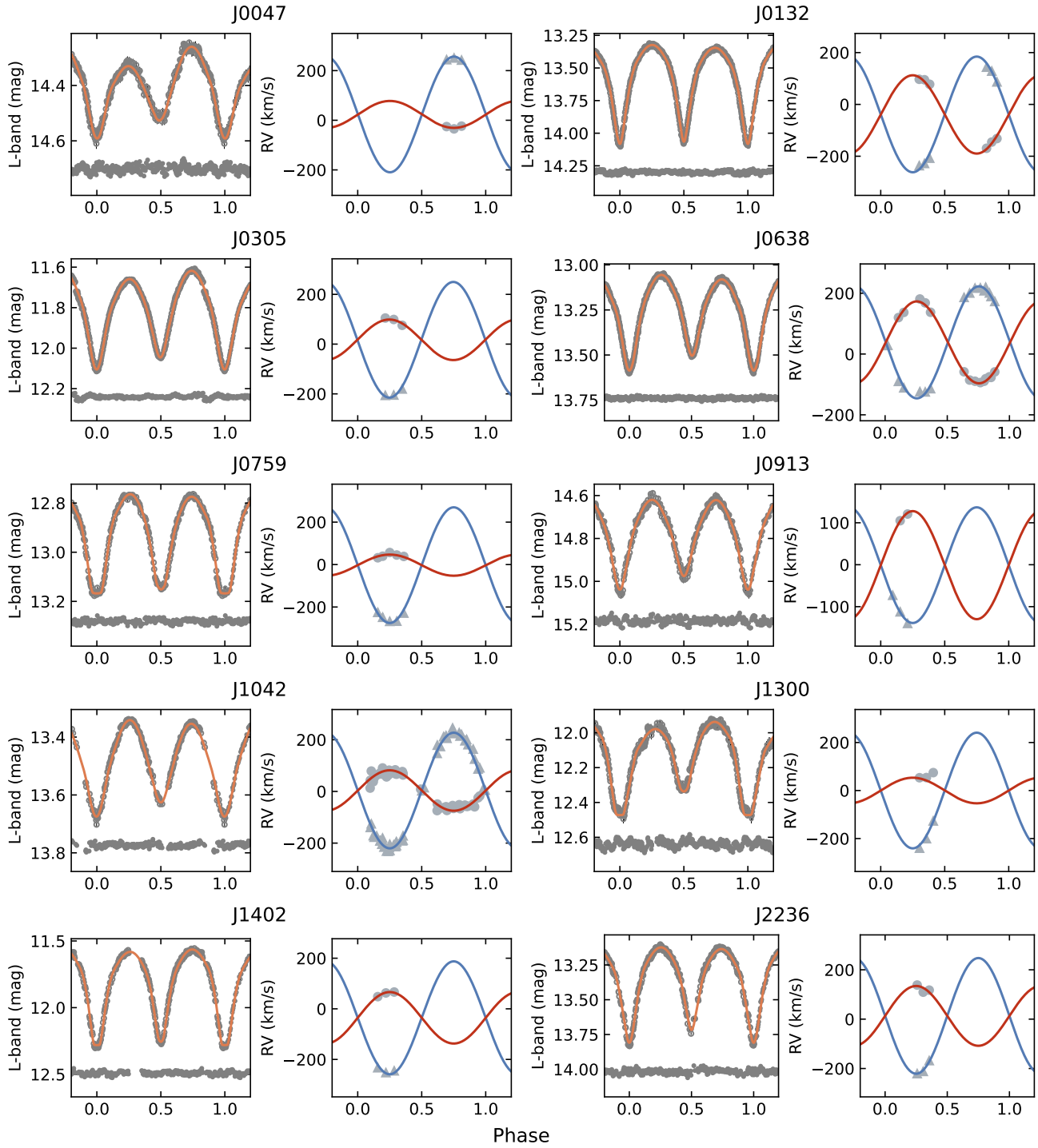


Figure 5. Left panel: Theoretical light curves (orange solid line) fitted by W-D code compared to all available TMTS observations (grey dots) for the ten targets. One dark spot is added to the primary or secondary star for each target. Right panel: RVs and fitted curves of W-D code. The grey filled triangles and circles represent the observed primary (hotter) and secondary (cooler) component, respectively. The blue and red solid lines represent the best-fit RV curves.

Table 7. Photometric solutions and absolute parameters of the ten targets

Parameter	J0047	J0132	J0305	J0638	J0759	J0913	J1042	J1300	J1402	J2236
$T_1(K)$	5113	6244	4822	5518	5144	5523	5652	5502	4544	5754
$T_2(K)$	4610 ± 19	6165 ± 6	4641 ± 7	5263 ± 6	4947 ± 9	5142 ± 22	5313 ± 23	4970 ± 15	4408 ± 23	5503 ± 16
$T_1-\sigma(K)$	58	158	26	26	81	24	21	28	49	27
$T_2-\sigma(K)$	56	156	26	25	78	31	31	30	48	30
$q(M_2/M_1)$	4.29 ± 0.05	1.48 ± 0.02	2.85 ± 0.01	1.37 ± 0.01	5.47 ± 0.04	1.07 ± 0.01	2.86 ± 0.05	4.51 ± 0.04	2.19 ± 0.05	1.93 ± 0.07
$i(deg)$	61.5 ± 0.2	83.5 ± 0.1	70.9 ± 0.1	71.6 ± 0.1	78.2 ± 0.3	66.9 ± 0.2	62.2 ± 0.3	78.7 ± 0.7	87.6 ± 0.3	79.5 ± 0.3
$V_\gamma(km/s)$	23.5 ± 2.1	-38.7 ± 3.1	17.4 ± 3.6	38.4 ± 1.3	-2.8 ± 2.2	-1.1 ± 1.5	3.5 ± 1.4	1.0 ± 4.6	-35.5 ± 1.4	13.2 ± 6.0
Ω_{in}	8.28	4.49	6.42	4.33	9.74	3.85	6.43	8.56	5.52	5.16
Ω_{out}	7.65	3.92	5.80	3.76	9.10	3.30	5.81	7.92	4.92	4.56
$\Omega_1 = \Omega_2$	8.13 ± 0.01	4.42 ± 0.03	6.26 ± 0.05	4.26 ± 0.01	9.75 ± 0.04	3.83 ± 0.02	6.26 ± 0.07	8.52 ± 0.05	5.44 ± 0.07	5.08 ± 0.10
L_{1L}/L_L	0.319 ± 0.003	0.422 ± 0.001	0.328 ± 0.002	0.485 ± 0.001	0.210 ± 0.001	0.567 ± 0.002	0.346 ± 0.004	0.294 ± 0.002	0.370 ± 0.004	0.402 ± 0.005
τ_1	0.273 ± 0.000	0.354 ± 0.000	0.307 ± 0.000	0.360 ± 0.000	0.250 ± 0.000	0.377 ± 0.000	0.308 ± 0.000	0.259 ± 0.000	0.320 ± 0.000	0.330 ± 0.001
τ_2	0.520 ± 0.001	0.425 ± 0.002	0.490 ± 0.002	0.416 ± 0.001	0.537 ± 0.001	0.387 ± 0.001	0.487 ± 0.003	0.516 ± 0.002	0.457 ± 0.003	0.448 ± 0.006
f	24.1 ± 2.3	12.8 ± 4.4	26.4 ± 8.1	14.5 ± 2.3	14.5 ± 5.9	2.6 ± 3.0	25.7 ± 10.7	6.2 ± 8.6	13.4 ± 10.7	12.6 ± 16.7
spot	Star 2	Star 1	Star 1	Star 1	Star 1	Star 1	Star 1	Star 1	Star 1	Star 1
Latitude($^\circ$)	90.0	90.0	90.0	90.0	90.0	90.0	90.0	90.0	90.0	90.0
Longitude($^\circ$)	70.2 ± 1.7	60.0 ± 3.2	268.9 ± 2.9	48.5 ± 2.1	110.9 ± 8.6	170.8 ± 5.5	48.3 ± 6.7	309.9 ± 4.2	303.9 ± 6.7	35.0 ± 6.4
Angular radius($^\circ$)	19.0 ± 0.3	14.1 ± 0.3	19.7 ± 0.3	14.8 ± 0.3	11.9 ± 1.0	9.3 ± 3.4	12.9 ± 0.6	24.2 ± 0.6	13.6 ± 0.6	12.6 ± 0.8
T-factor	0.66 ± 0.04	0.72 ± 0.02	0.70 ± 0.02	0.70 ± 0.02	0.70 ± 0.07	0.80 ± 0.15	0.70 ± 0.05	0.70 ± 0.03	0.80 ± 0.05	0.78 ± 0.04
$\Sigma(O-C)^2$	6.0×10^{-9}	8.8×10^{-9}	4.0×10^{-8}	8.9×10^{-9}	1.7×10^{-8}	5.1×10^{-9}	8.4×10^{-9}	9.6×10^{-8}	7.1×10^{-8}	1.6×10^{-8}
$\Delta m(\text{observed})$	0.069	-0.022	0.040	-0.025	-0.010	-0.001	-0.013	0.046	0.018	-0.013
b-factor ₁	4.3	3.6	4.6	4.0	4.3	4.0	3.9	4.0	4.9	3.9
b-factor ₂	4.8	3.6	4.8	4.2	4.5	4.3	4.2	4.5	5.0	4.0
$\Delta m(\text{Doppler-boosting})$	-0.005	-0.002	-0.005	-0.001	-0.007	0.000	-0.004	-0.005	-0.004	-0.003
Absolute parameters										
$a(R_\odot)$	1.69 ± 0.03	2.98 ± 0.02	1.62 ± 0.04	2.35 ± 0.02	1.93 ± 0.02	1.60 ± 0.01	2.21 ± 0.02	1.79 ± 0.07	1.68 ± 0.02	2.40 ± 0.06
$M_1(M_\odot)$	0.179 ± 0.012	0.897 ± 0.022	0.244 ± 0.019	0.590 ± 0.020	0.170 ± 0.007	0.285 ± 0.006	0.338 ± 0.017	0.153 ± 0.018	0.291 ± 0.017	0.561 ± 0.059
$M_2(M_\odot)$	0.768 ± 0.060	1.325 ± 0.047	0.695 ± 0.064	0.807 ± 0.033	0.926 ± 0.047	0.422 ± 0.015	0.967 ± 0.065	0.692 ± 0.089	0.638 ± 0.065	1.084 ± 0.155
$R_1(R_\odot)$	0.464 ± 0.009	1.065 ± 0.007	0.502 ± 0.012	0.855 ± 0.009	0.484 ± 0.006	0.568 ± 0.003	0.661 ± 0.008	0.468 ± 0.018	0.541 ± 0.008	0.799 ± 0.023
$R_2(R_\odot)$	0.880 ± 0.018	1.269 ± 0.012	0.794 ± 0.022	0.984 ± 0.012	1.034 ± 0.016	0.678 ± 0.006	1.046 ± 0.018	0.926 ± 0.035	0.770 ± 0.018	1.075 ± 0.042
$L_1(L_\odot)$	0.132 ± 0.005	1.556 ± 0.022	0.123 ± 0.006	0.611 ± 0.013	0.148 ± 0.004	0.270 ± 0.003	0.402 ± 0.010	0.181 ± 0.014	0.113 ± 0.010	0.631 ± 0.036
$L_2(L_\odot)$	0.316 ± 0.013	2.098 ± 0.041	0.264 ± 0.015	0.670 ± 0.016	0.578 ± 0.018	0.290 ± 0.006	0.787 ± 0.027	0.472 ± 0.036	0.202 ± 0.027	0.955 ± 0.075
$\log J_{orb}$	51.045 ± 0.018	51.921 ± 0.003	51.129 ± 0.020	51.572 ± 0.005	51.010 ± 0.010	51.053 ± 0.007	51.403 ± 0.010	50.970 ± 0.034	51.179 ± 0.017	51.647 ± 0.016

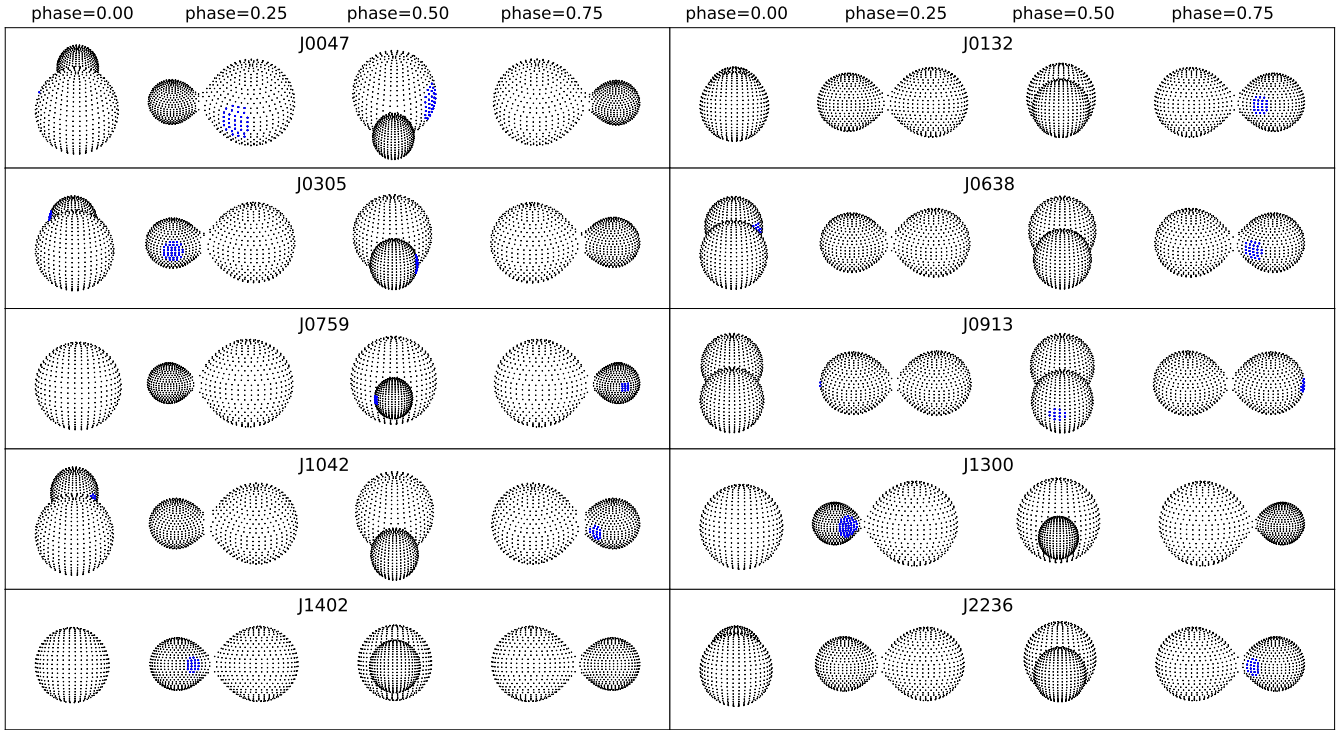


Figure 6. Geometrical structures of ten targets at phase 0, 0.25, 0.5, and 0.75. The areas marked with blue cross symbols represent the added dark spots on the components.

4.2. Spectroscopic Investigation

When the photosphere or chromosphere of a star exhibits magnetic activity, the atmosphere of the star is heated non-thermally by the magnetic field. The spectral subtraction technique is usually used to investigate chromospheric activity (Barden 1985). The activity is quantified by the equivalent width (EW) of the emission line, such as the Balmer series ($H\alpha$, $H\beta$, $H\gamma$) and the Ca II infrared triplet (IRT), which serve as useful indicators of chromospheric activity in many contact binaries (Pavlenko et al. 2018; Li et al. 2022; Liu et al. 2023b; Li et al. 2024a).

We analyzed the LAMOST LR spectra for these ten targets to assess their chromospheric activities. Excluding J0132 and J0913, there are a total of 14 spectra for 8 targets. The analysis process follows three fundamental steps. Firstly, based on the temperatures of the two components obtained from the W-D solution for each target, we selected template spectra for the primary and secondary stars from the radial velocity standard star catalog of Huang et al. (2018). The temperatures of the inactive template spectra were chosen to closely match the components of binary, with a difference not exceeding 200 K. Secondly, we downloaded these template spectra from LAMOST DR10, removing the cosmic rays and normalizing the spectra. Thirdly, the Fortran code STARMOD was used to construct the synthetic spectra of the binaries, taking into account the radial velocity, the rotationally broadening, and the relative weight of the two components. The values for the radial velocity and rotationally broadening were referenced from the LAMOST LR spectra, while the weights of the two components were derived from the W-D solution. These parameters were also treated as free during the STARMOD process. Finally, the subtracted spectra between the LAMOST observed spectra and the synthetic spectra were obtained and displayed in Figure 7, showing only the $H\alpha$ region.

The blue lines in Figure 7 represent the subtracted spectra, which show the varying intensities of the emission lines. We used the Python package *PySpecKit* to calculate the EWs of the $H\alpha$ emission lines, which are listed in Table 2. In previous studies, stars with EW of $H\alpha$ greater than 0.75\AA were considered magnetically active (West et al. 2011, 2015). Therefore, we infer that J0047, J0305, J0638, and J1402 exhibit strong magnetic activities.

5. DISCUSSION

5.1. Orbital and Absolute Physical Parameters

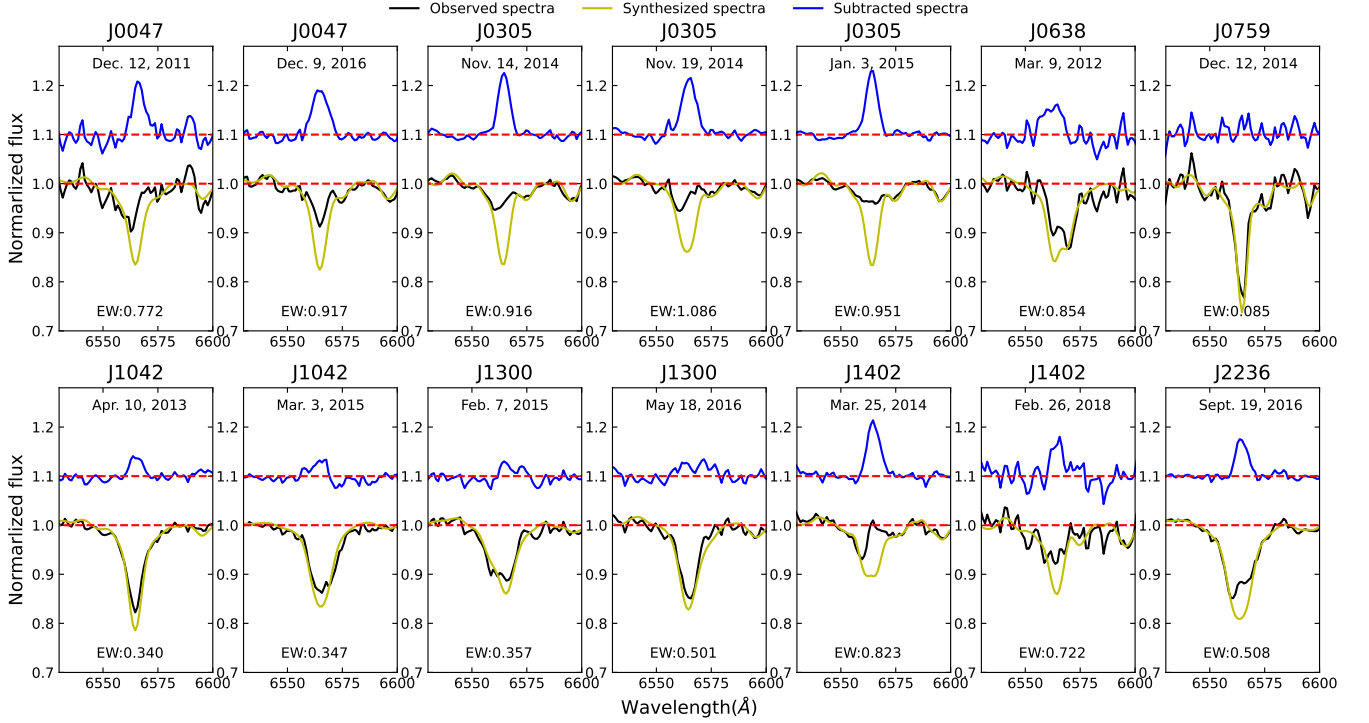


Figure 7. The $H\alpha$ region of LAMOST LR spectra (black line), synthetic spectra (yellow line) and subtracted spectra (blue line) for the eight targets. The EWs of $H\alpha$ are shown in each panel for each spectra, with units in \AA .

According to the W-D code DC and LC program, the orbital and absolute physical parameters of the ten targets were determined, including the mass ratio q , inclination i , fill-out factor f , semi-major axis a , masses of the two components (M_1 , M_2), radii of the two components (R_1 , R_2). The luminosities of two components (L_1 , L_2) are determined by the Stefan-Boltzmann law. All orbital and absolute physical parameters are tabulated in Table 7. The RV data for these ten targets have been obtained for the first time. Note that four of them have been systematically analyzed in previous studies, with their physical parameters being estimated. Each of these four targets will be discussed below.

(i) For J0132, Liu & Tan (1991) reported a mass ratio of 0.5947 (M_2/M_1), and Kjurkchieva et al. (2019) gave a value of 0.635 (M_2/M_1). In this work, the mass ratio was determined as 0.676 (M_1/M_2).

(ii) For J0305, Panchal & Joshi (2021) reported a mass ratio of 0.31 (M_2/M_1), and our analysis gives a value of 0.35 (M_1/M_2).

(iii) For J1300, the mass ratios previously determined by Kjurkchieva et al. (2018) and Yang et al. (2023) were 4.66 (M_2/M_1) and 4.747 (M_2/M_1), respectively, which are approximately the same as the value of 4.51 (M_2/M_1) obtained in this work.

(iv) For J1402, Yang (2011) and Alton & Stepień (2021) reported mass ratios of 0.461 (M_1/M_2) and 0.443 (M_1/M_2), respectively. The mass ratio of 0.457 (M_1/M_2) determined in this study is also consistent with their results.

Therefore, the mass ratios obtained for these four targets in our study are generally consistent with those reported in previous works. For J0132 and J0305, the temperatures of the two components may have been assigned to different components due to their small temperature differences.

5.2. The Variation of the Orbital Period

With the LC minima collected from superWASP, TESS, ZTF, ASAS, CSS, ASAS-SN, BRNO, TMTS, and other literature, we analyzed orbital period variations for the targets. The final analysis revealed that all targets provided the corrected initial epochs and orbital periods. Except for J1042, the periods of the other nine targets exhibit a long-term increasing or decreasing trend, with three targets also showing cyclic period variations.

The long-term period decrease or increase can probably be explained by the mass transfer between two components. Assuming the conservation of mass and angular momentum, we used the following equation to calculate the rate of

mass transfer,

$$\frac{\dot{P}}{P} = -3\dot{M}_1 \left(\frac{1}{M_1} - \frac{1}{M_2} \right). \quad (3)$$

By combining the period change \dot{P} (dp/dt) of each target and the masses of the two components provided in Tables 5 and 7, we calculated the \dot{M}_1 (dM_1/dt , rate of mass transfer) for each target, which are listed in Table 5. The positive value indicates that the primary star M_1 is receiving mass, while the negative value indicates that the primary star M_1 is losing mass.

A long-term decreasing period is caused by mass transfer from the more massive star to the less massive star. This explanation is applied to J0047, J0638, and J1402. Therefore, we calculated the timescale of mass transfer ($\tau_{mt} \sim \frac{M_{1,2}}{M_{1,2}}$) and the thermal timescale ($\tau_{tt} \sim \frac{GM^2}{RL}$) for these three targets, and listed in Table 8.

Table 8. The mass transfer timescale and thermal timescale for J0047, J0638, and J1402.

Name	$\frac{M_{1,2}}{M_{1,2}} \times 10^7$ yr	$\frac{GM^2}{RL} \times 10^7$ yr
J0047	0.21	5.20
J0638	0.10	9.85
J1402	0.43	26.18

The two timescales for these three targets differ significantly, with the mass transfer timescale being 4.00%, 1.04%, and 1.64% of the thermal timescale, respectively. Therefore, mass transfer cannot explain the long-term decrease in period for J0047, J0638, and J1402. The long-term period decrease in these targets is probably due to angular momentum loss (AML). Furthermore, the possibility that O-C of J0047 and J0638 is part of a cyclic variation cannot be ruled out.

For the other seven targets, the long-term increasing trend of the period may be due to mass transfer from the less massive star to the more massive one. Due to the conservation of angular momentum, the distance between the two components increases as their mass transfer, leading to a decrease in the degree of contact. The systems will evolve from the current contact state to a semi-detached or detached state. According to stellar evolution theory, the more massive star will fill its Roche lobe first. As a result, the mass will be transferred from the more massive star to the less massive one. The mass and energy are then exchanged between the two components, leading to the evolution towards a contact state again. This is called as the thermal relaxation oscillation model (TRO) of contact binaries (Lucy 1976; Flannery 1976; Robertson & Eggleton 1977). Therefore, long-term monitoring of these targets is necessary in the future.

The cyclic variation of the $O - C$ parameter can be explained by the light travel-time effect (LTTE) due to the presence of a companion star or by a magnetic activity cycle. The existence of a third body is often used to explain the cyclic variation of orbital period, such as BK Vul (Adalahi & Soydugan 2024); CW Aqr (Vijaya & Sriram 2023); CSS_J154915.7+375506 (Wu et al. 2024). If J0132, J1300, and J1402 are in triple systems, we can apply the function below to describe them:

$$f(m) = \frac{4\pi}{GP_3^2} \times (a'_{12} \sin i')^3 = \frac{(M_3 \sin i')^3}{(M_1 + M_2 + M_3)^2}, \quad (4)$$

where G and P_3 are the gravitational constant and the period of the $(O - C)_2$ oscillation, respectively. The amplitude of the oscillation is $A = \frac{a'_{12} \sin i'}{c} \sqrt{1 - e'^2 \cos^2 \omega'}$, where a'_{12} is the distance between binary and barycenter of the triple body system, c is the speed of light and i' is the inclination of the orbit of the third component. M_1 and M_2 represent the mass of the two components, and M_3 is the mass of the third body. We determined $f(m)$ of the additional component for the three targets. The orbital distance between the third body and the central binary can be estimated as $a_3 = (M_1 + M_2) \times a_{12}/M_3$. If the orbital inclination of the third body i' is the same as the binaries ($i' = i$) for the three targets, respectively, the mass and the distance of the tertiary companion are calculated. All parameters are listed in Table 6. Therefore, if the third body is a main sequence star, the spectral type and the luminosity were determined according to the relation of Cox (2000). Finally, the M_3 of J0132 is too small for it to be a main sequence

star and may be a brown dwarf. The spectral type and the proportion of the third body to the total luminosity for J1300 and J1402 are determined and listed in Table 6.

Another possible mechanism is magnetic activity. The Applegate mechanism (Applegate 1992) involves magnetic activity that produces a change in the variation of the quadrupole moment and, finally, the change in the orbital period. This can be described by using the following equation (Lanza & Rodonò 2002),

$$\frac{\Delta P}{P} = -9 \frac{\Delta Q}{Ma^2}, \quad (5)$$

where ΔP is the period of cyclic variation, P is the orbital period, M is the mass for each component of the binary system, and a is the semi-major axis of binary system. The quadrupole momenta of the required variation of both components (ΔQ_1 and ΔQ_2) were determined and tabulated in Table 6. The typical value is usually 10^{51} to 10^{52} g cm² for close binaries (Lanza & Rodonò 1999), and $\Delta Q = 10^{49}$ g cm² for cataclysmic variables (Lanza & Rodonò 1999). Although the quadrupole momenta of many binaries are not in agreement with the typical value, such as DZ Psc (Yang et al. 2013), V1101 Her (Pi et al. 2017), V0474 Cam (Guo et al. 2018). They are all similar with the value of 10^{49} g cm². Thus, we cannot exclude the possibility of magnetic activity, especially for J1402. The light curve of J1402 exhibits the O’Connell effect and its spectra show strong magnetic activity.

Therefore, the periodic change for J1300 and J1402 may be caused by the existence of a dim third body, but the Applegate mechanism cannot be excluded because both show evidence of magnetic activity. The cyclic variation of $O - C$ for J0132 may be due to magnetic activity. More observational data are needed in the future to confirm this.

5.3. Evolutionary State

With the absolute physical parameters, the positions of binaries on the mass-luminosity (M-L) and mass-radius (M-R) diagrams can be determined. In Figure 8, the solid and dotted lines show the zero age main sequence (ZAMS) and the terminal age main sequence (TAMS), constructed with the help of the binary star evolution code (BSE) (Hurley et al. 2002).

The more massive stars of all binary sample except J0132 and J0913 are located between the ZAMS line and the TAMS line, while the less massive stars are located above the TAMS line. This indicates that the currently more massive star is a main sequence star, and the currently less massive star is over-luminous and oversized relative to main sequence counterparts with the same mass. This excess in luminosity and radius may be explicable by developments in the early evolution of the system. For J0132, both components are located in the main sequence, while for J0913, both components are above the TAMS. This suggests that these two targets may have evolved more slowly or more rapidly compared to the other eight targets.

Following Christopoulou & Papageorgiou (2013), we used the equation below to describe the relationship between mass and angular momentum J_{orb} of contact binaries:

$$J_{orb} = 1.24 \times 10^{52} \times M_T^{3/5} \times P^{1/3} \times q \times (1 + q)^{-2}, \quad (6)$$

where J_{orb} , M_T , P , and q represent the angular momentum, total mass of the binary system, orbital period, and the mass ratio, respectively. Combining the values of these parameters, the angular momentum of these ten targets was determined and listed in Table 7. The relationship of M_T and J_{orb} for detached binaries and overcontact binaries is shown in Figure 9, where the boundary line separates detached binaries and overcontact binaries. Note that the data for the detached binaries in the sample were collected from Eker et al. (2006), while the data for overcontact binaries were collected from Eker et al. (2006) and Yakut & Eggleton (2005). The positions of ten targets are marked in Figure 9. It can be seen that all targets are below the boundary line, and J0132 and J0913 are very close to it. Many researchers have proposed that the W UMa binaries may be formed from short period detached binaries by AML (e.g. Stepień 2006; Stepień 2011; Yıldız & Doğan 2013; Yıldız 2014; Qian et al. 2017). Considering their positions on the M-L and M-R diagrams in Figure 8, along with the overall trends and their low fill-out factors, we infer that these two targets may be newly formed contact binaries.

6. SUMMARY

Through the TMTS photometric observations and the LAMOST MR spectroscopic observations of the ten targets, physical parameters were obtained from the W-D analysis. The unequal two maxima of the light curves for every target indicate that the O’Connell effect is significant. We adopted the photometric solution with the spot of all targets as the

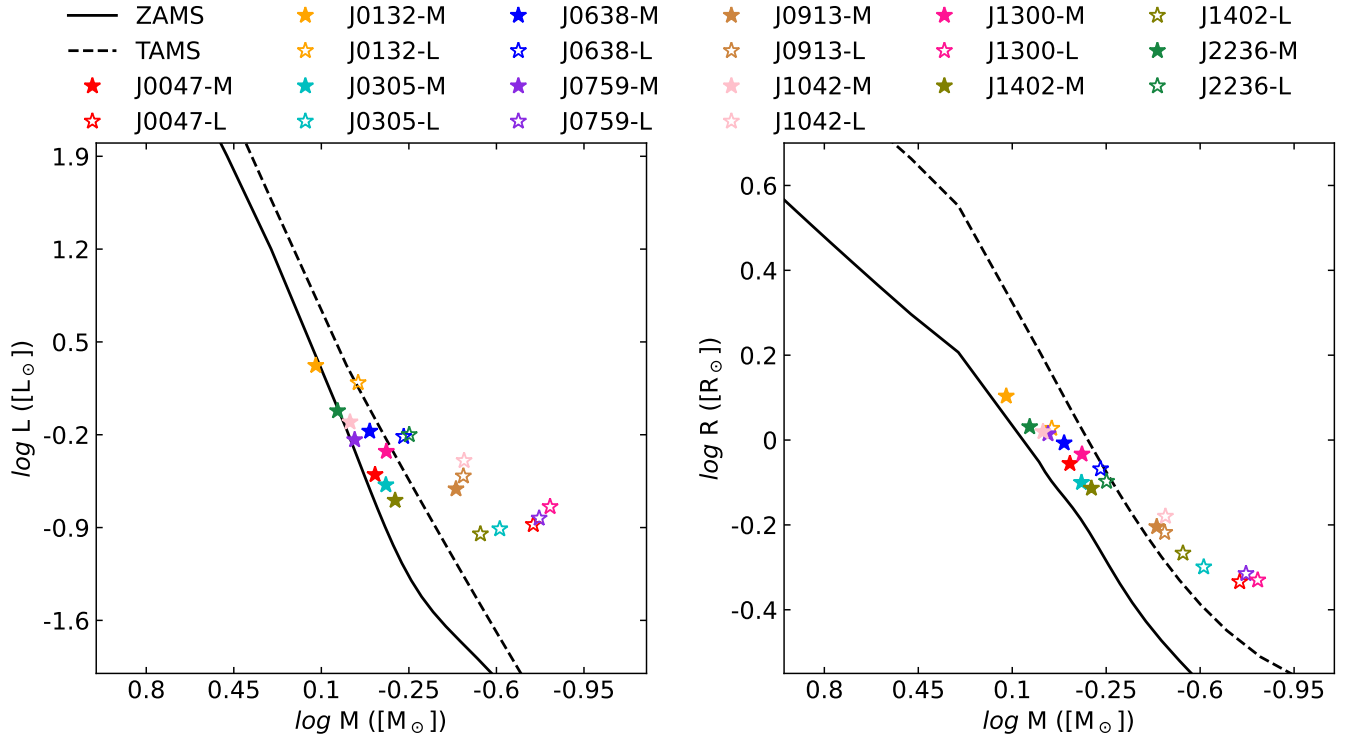


Figure 8. Mass-luminosity diagram (left panel) and mass-radius diagram (right panel). The solid and dotted lines represent the ZAMS and TAMS lines constructed using the binary star evolution code provided by Hurley et al. (2002). The solid and open stars for different colors represent the more massive star (M) and less massive star (L) of the ten targets, respectively.

final result. The ten targets are determined to be all W-type contact binaries, in which J0047, J0305, and J1042 are the median contact binaries and the others are shallow contact binaries. Based on all available minima, we analyzed the period change for the ten targets and obtained a long-term increasing or decreasing component. J0132, J1300, and J1402 exhibit cyclic variations for the orbital period, which may be due to their presence in a triple system. Based on spectroscopic analysis, J0047, J0305, J0638, and J1402 exhibit strong magnetic activity. The evolutionary states of J0132 and J0913 differ from the other eight targets. Considering their low fill-out factors and relatively high angular momenta, these two targets may be newly formed contact binaries resulting from AML.

In the forthcoming papers, we will construct training and test datasets, employing machine learning methods to publish a catalog of physical parameters for a large sample of contact binaries. For the interesting targets obtained, phenomena such as low-mass ratios and short-period cutoffs will be discussed and studied in detail. For contact binaries in future TMTS observations, we will continue to obtain their radial velocity data from LAMOST or other surveys as much as possible, enriching and expanding the entire database of absolute physical parameters for contact binaries.

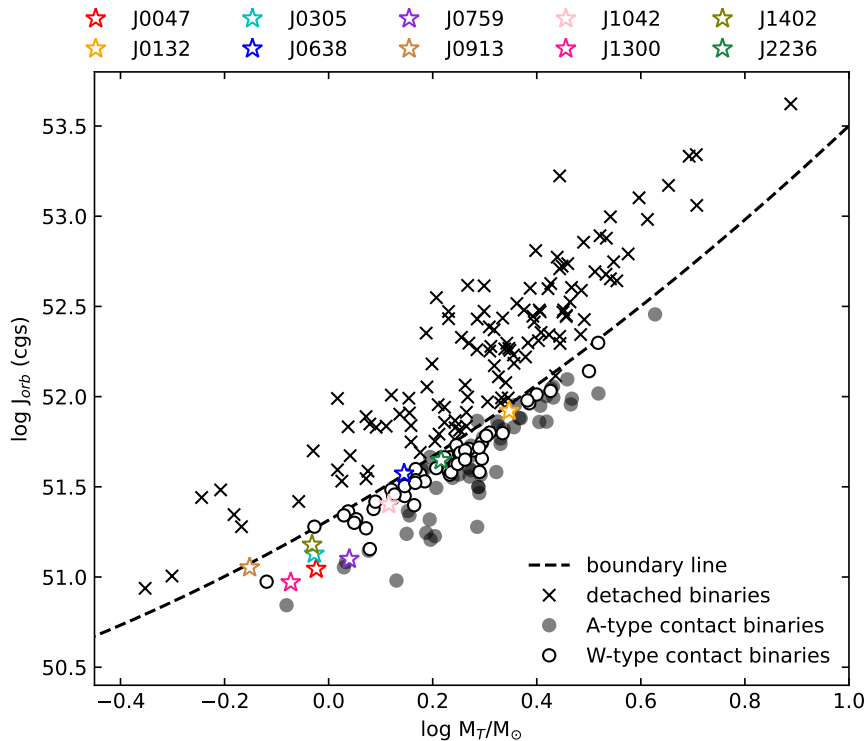


Figure 9. The relation between orbital angular momentum and total mass for detached and contact binaries. The detached binaries (Eker et al. 2006) and the contact binary (Yakut & Eggleton 2005; Eker et al. 2006) are separated by the boundary line (Eker et al. 2006). The black crosses represent the detached binaries, the black solid and open circles refer to the A-type and W-type contact binaries, respectively. Different colored stars represent different targets.

We acknowledge the support of the staff of the Xinglong Observatory of National Astronomical Observatories of China (NAOC) during the installation, commissioning and operation of the Tsinghua University-Ma Huateng Telescopes for Survey (TMTS) system. This work is supported by the National Science Foundation of China (NSFC grants 12033003 and 12288102), the Ma Huateng Foundation, the Scholar Program of Beijing Academy of Science and Technology (DZ:BS202002), the Tencent Xplorer Prize, Beijing Natural Science Foundation (No. 1242016), and the Talents Program (24CE-YS-08) of Beijing Academy of Science and Technology. J. L. is supported by the National Natural Science Foundation of China (NSFC; Grant Numbers 12403038), the Fundamental Research Funds for the Central Universities (Grant Numbers WK2030000089), and the Cyrus Chun Ying Tang Foundations.

Guoshoujing Telescope (the Large Sky Area Multi-Object Fiber Spectroscopic Telescope LAMOST) is a National Major Scientific Project built by the Chinese Academy of Sciences. Funding for the project has been provided by the National Development and Reform Commission. LAMOST is operated and managed by the National Astronomical Observatories, Chinese Academy of Sciences.

This work has made use of data from the European Space Agency (ESA) mission *Gaia* (<https://www.cosmos.esa.int/gaia>), processed by the *Gaia* Data Processing and Analysis Consortium (DPAC, <https://www.cosmos.esa.int/web/gaia/dpac/consortium>). Funding for the DPAC has been provided by national institutions, in particular the institutions participating in the *Gaia* Multilateral Agreement.

This research has made use of the International Variable Star Index (VSX, Watson et al. 2006) data base, operated at the American Association of Variable Star Observers (AAVSO), Cambridge, Massachusetts, USA. Some of the results in this paper have been derived using the HEALPIX (Górski et al. 2005) package.

We acknowledge the use of data from the SuperWASP project, TESS (Transiting Exoplanet Survey Satellite), ZTF (Zwicky Transient Facility), ASAS (All Sky Automated Survey), CSS (Catalina Sky Survey), ASAS-SN (All-Sky Automated Survey for Supernovae), and Brno Regional Network of Observers (B.R.N.O.). These resources and efforts have been invaluable to this study and we sincerely thank the teams and organizations for their publicly available data and continuous efforts.

REFERENCES

- Adalah, S., & Soydugan, E. 2024, *NewA*, 112, 102270, doi: [10.1016/j.newast.2024.102270](https://doi.org/10.1016/j.newast.2024.102270)
- Akerlof, C., Amrose, S., Balsano, R., et al. 2000, *AJ*, 119, 1901, doi: [10.1086/301321](https://doi.org/10.1086/301321)
- Alton, K. B., & Stepień, K. 2021, *AcA*, 71, 123, doi: [10.32023/0001-5237/71.2.4](https://doi.org/10.32023/0001-5237/71.2.4)
- Alvarez, G. E., Sowell, J. R., Williamon, R. M., & Lapasset, E. 2015, *PASP*, 127, 742, doi: [10.1086/682388](https://doi.org/10.1086/682388)
- Applegate, J. H. 1992, *ApJ*, 385, 621, doi: [10.1086/170967](https://doi.org/10.1086/170967)
- Barden, S. C. 1985, *ApJ*, 295, 162, doi: [10.1086/163361](https://doi.org/10.1086/163361)
- Baron, E., & Hauschildt, P. H. 2007, *A&A*, 468, 255, doi: [10.1051/0004-6361:20066755](https://doi.org/10.1051/0004-6361:20066755)
- Bellm, E. C., Kulkarni, S. R., Graham, M. J., et al. 2019, *PASP*, 131, 018002, doi: [10.1088/1538-3873/aaecbe](https://doi.org/10.1088/1538-3873/aaecbe)
- Berdyugina, S. V. 2005, *Living Reviews in Solar Physics*, 2, 8, doi: [10.12942/lrsp-2005-8](https://doi.org/10.12942/lrsp-2005-8)
- Binnendijk, L. 1970, *Vistas in Astronomy*, 12, 217, doi: [10.1016/0083-6656\(70\)90041-3](https://doi.org/10.1016/0083-6656(70)90041-3)
- Blattler, E., & Diethelm, R. 2003, *Information Bulletin on Variable Stars*, 5403, 1
- Christopoulou, P. E., & Papageorgiou, A. 2013, *AJ*, 146, 157, doi: [10.1088/0004-6256/146/6/157](https://doi.org/10.1088/0004-6256/146/6/157)
- Christy, C. T., Jayasinghe, T., Stanek, K. Z., et al. 2023, *MNRAS*, 519, 5271, doi: [10.1093/mnras/stac3801](https://doi.org/10.1093/mnras/stac3801)
- Cox, A. N. 2000, *Allen's astrophysical quantities*
- Cui, X.-Q., Zhao, Y.-H., Chu, Y.-Q., et al. 2012, *Research in Astronomy and Astrophysics*, 12, 1197, doi: [10.1088/1674-4527/12/9/003](https://doi.org/10.1088/1674-4527/12/9/003)
- Deb, S., & Singh, H. P. 2011, *MNRAS*, 412, 1787, doi: [10.1111/j.1365-2966.2010.18016.x](https://doi.org/10.1111/j.1365-2966.2010.18016.x)
- Demircan, Y., Gurol, B., Gokay, G., et al. 2011, *Information Bulletin on Variable Stars*, 5965, 1
- Diethelm, R. 2005, *Information Bulletin on Variable Stars*, 5653, 1
- . 2006, *Information Bulletin on Variable Stars*, 5713, 1
- . 2007, *Information Bulletin on Variable Stars*, 5781, 1
- . 2009a, *Information Bulletin on Variable Stars*, 5871, 1
- . 2009b, *Information Bulletin on Variable Stars*, 5894, 1
- . 2010a, *Information Bulletin on Variable Stars*, 5920, 1
- . 2010b, *Information Bulletin on Variable Stars*, 5945, 1
- . 2011a, *Information Bulletin on Variable Stars*, 5960, 1
- . 2011b, *Information Bulletin on Variable Stars*, 5992, 1
- . 2012a, *Information Bulletin on Variable Stars*, 6011, 1
- . 2012b, *Information Bulletin on Variable Stars*, 6029, 1
- Ding, X., Ji, K., Li, X., et al. 2023, *MNRAS*, 525, 4596, doi: [10.1093/mnras/stad2565](https://doi.org/10.1093/mnras/stad2565)
- Ding, X., Ji, K.-F., & Li, X.-Z. 2021, *PASJ*, 73, 786, doi: [10.1093/pasj/psab042](https://doi.org/10.1093/pasj/psab042)
- Dvorak, S. W. 2005, *Information Bulletin on Variable Stars*, 5603, 1
- Eker, Z. 1999, *Turkish Journal of Physics*, 23, 357
- Eker, Z., Demircan, O., Bilir, S., & Karataş, Y. 2006, *MNRAS*, 373, 1483, doi: [10.1111/j.1365-2966.2006.11073.x](https://doi.org/10.1111/j.1365-2966.2006.11073.x)
- Flannery, B. P. 1976, *ApJ*, 205, 217, doi: [10.1086/154266](https://doi.org/10.1086/154266)
- Gaia Collaboration, Prusti, T., de Bruijne, J. H. J., et al. 2016, *A&A*, 595, A1, doi: [10.1051/0004-6361/201629272](https://doi.org/10.1051/0004-6361/201629272)
- Gaia Collaboration, Brown, A. G. A., Vallenari, A., et al. 2018, *A&A*, 616, A1, doi: [10.1051/0004-6361/201833051](https://doi.org/10.1051/0004-6361/201833051)
- Gessner, H., & Meinunger, I. 1973, *Veroeffentlichungen der Sternwarte Sonneberg*, 7, 607
- Górski, K. M., Hivon, E., Banday, A. J., et al. 2005, *ApJ*, 622, 759, doi: [10.1086/427976](https://doi.org/10.1086/427976)
- Guo, D. F., Li, K., Hu, S. M., & Chen, X. 2018, *PASP*, 130, 064201, doi: [10.1088/1538-3873/aaba50](https://doi.org/10.1088/1538-3873/aaba50)
- Guo, F., Lin, J., Wang, X., et al. 2024, *MNRAS*, 528, 6997, doi: [10.1093/mnras/stae404](https://doi.org/10.1093/mnras/stae404)
- Guo, Y.-N., Li, K., Xia, Q.-Q., et al. 2020, *Research in Astronomy and Astrophysics*, 20, 179, doi: [10.1088/1674-4527/20/11/179](https://doi.org/10.1088/1674-4527/20/11/179)
- Hauschildt, P. H. 1993, *JQSRT*, 50, 301, doi: [10.1016/0022-4073\(93\)90080-2](https://doi.org/10.1016/0022-4073(93)90080-2)
- Hauschildt, P. H., & Baron, E. 2006, *A&A*, 451, 273, doi: [10.1051/0004-6361:20053846](https://doi.org/10.1051/0004-6361:20053846)
- Heinze, A. N., Tonry, J. L., Denneau, L., et al. 2018, *AJ*, 156, 241, doi: [10.3847/1538-3881/aae47f](https://doi.org/10.3847/1538-3881/aae47f)
- Hoffman, D. I., Harrison, T. E., & McNamara, B. J. 2009, *AJ*, 138, 466, doi: [10.1088/0004-6256/138/2/466](https://doi.org/10.1088/0004-6256/138/2/466)
- Hoffmeister, C. 1966, *Astronomische Nachrichten*, 289, 139, doi: [10.1002/asna.19662890306](https://doi.org/10.1002/asna.19662890306)
- Honková, K., Juryšek, J., Lehký, M., et al. 2014, *Open European Journal on Variable Stars*, 165, 1
- Honkova, K., Jurysek, J., Lehky, M., et al. 2015, *Open European Journal on Variable Stars*, 168, 1, doi: [10.48550/arXiv.1606.00369](https://doi.org/10.48550/arXiv.1606.00369)
- Hoňková, K., Juryšek, J., Lehký, M., et al. 2013, *Open European Journal on Variable Stars*, 160, 1
- Hrivnak, B. J. 1988, *ApJ*, 335, 319, doi: [10.1086/166930](https://doi.org/10.1086/166930)
- . 1989, *ApJ*, 340, 458, doi: [10.1086/167408](https://doi.org/10.1086/167408)
- Huang, Y., Liu, X. W., Chen, B. Q., et al. 2018, *AJ*, 156, 90, doi: [10.3847/1538-3881/aacda5](https://doi.org/10.3847/1538-3881/aacda5)
- Hubscher, J. 2005, *Information Bulletin on Variable Stars*, 5643, 1
- . 2014, *Information Bulletin on Variable Stars*, 6118, 1
- . 2017, *Information Bulletin on Variable Stars*, 6196, 1, doi: [10.22444/IBVS.6196](https://doi.org/10.22444/IBVS.6196)

- Hubscher, J., Braune, W., & Lehmann, P. B. 2013, *Information Bulletin on Variable Stars*, 6048, 1
- Hubscher, J., & Lehmann, P. B. 2012, *Information Bulletin on Variable Stars*, 6026, 1
- Hubscher, J., Lehmann, P. B., Monninger, G., Steinbach, H.-M., & Walter, F. 2010a, *Information Bulletin on Variable Stars*, 5941, 1
- . 2010b, *Information Bulletin on Variable Stars*, 5918, 1
- Hubscher, J., Lehmann, P. B., & Walter, F. 2012, *Information Bulletin on Variable Stars*, 6010, 1
- Hubscher, J., & Monninger, G. 2011, *Information Bulletin on Variable Stars*, 5959, 1
- Hubscher, J., Paschke, A., & Walter, F. 2005, *Information Bulletin on Variable Stars*, 5657, 1
- . 2006, *Information Bulletin on Variable Stars*, 5731, 1
- Hubscher, J., Steinbach, H.-M., & Walter, F. 2008, *Information Bulletin on Variable Stars*, 5830, 1
- Hurley, J. R., Tout, C. A., & Pols, O. R. 2002, *MNRAS*, 329, 897, doi: [10.1046/j.1365-8711.2002.05038.x](https://doi.org/10.1046/j.1365-8711.2002.05038.x)
- Irwin, J. B. 1952, *ApJ*, 116, 211, doi: [10.1086/145604](https://doi.org/10.1086/145604)
- Juryšek, J., Hoňková, K., Šmelcer, L., et al. 2017, *Open European Journal on Variable Stars*, 179, 1
- Kjurkchieva, D. P., Popov, V. A., Eneva, Y., & Petrov, N. I. 2019, *Research in Astronomy and Astrophysics*, 19, 014, doi: [10.1088/1674-4527/19/1/14](https://doi.org/10.1088/1674-4527/19/1/14)
- Kjurkchieva, D. P., Popov, V. A., Lyubenova Vasileva, D., & Petrov, N. I. 2018, *Research in Astronomy and Astrophysics*, 18, 046, doi: [10.1088/1674-4527/18/4/46](https://doi.org/10.1088/1674-4527/18/4/46)
- Kwee, K. K., & van Woerden, H. 1956, *BAN*, 12, 327
- Lampens, P., Van Cauteren, P., Ayiomamitis, A., et al. 2017, *Information Bulletin on Variable Stars*, 6230, 1, doi: [10.22444/IBVS.6230](https://doi.org/10.22444/IBVS.6230)
- Lanza, A. F., & Rodonò, M. 1999, *A&A*, 349, 887
- . 2002, *Astronomische Nachrichten*, 323, 424, doi: [10.1002/1521-3994\(200208\)323:3/4<424::AID-ASNA424>3.0.CO;2-1](https://doi.org/10.1002/1521-3994(200208)323:3/4<424::AID-ASNA424>3.0.CO;2-1)
- Latković, O., Čeki, A., & Lazarević, S. 2021, *ApJS*, 254, 10, doi: [10.3847/1538-4365/abeb23](https://doi.org/10.3847/1538-4365/abeb23)
- Lee, J. W., & Park, J.-H. 2018, *PASP*, 130, 034201, doi: [10.1088/1538-3873/aaa390](https://doi.org/10.1088/1538-3873/aaa390)
- Lehký, M., Hoňková, K., Šmelcer, L., et al. 2021, *Open European Journal on Variable Stars*, 211, 1, doi: [10.5817/OEJV2021-0211](https://doi.org/10.5817/OEJV2021-0211)
- Lewandowski, M., Niedzielski, A., & Maciejewski, G. 2007, *Information Bulletin on Variable Stars*, 5784, 1
- Li, K. 2018, *NewA*, 59, 60, doi: [10.1016/j.newast.2017.09.004](https://doi.org/10.1016/j.newast.2017.09.004)
- Li, K., Gao, X., Liu, X.-Y., et al. 2022, *AJ*, 164, 202, doi: [10.3847/1538-3881/ac8ff2](https://doi.org/10.3847/1538-3881/ac8ff2)
- Li, K., Hu, S. M., Guo, D. F., et al. 2015, *AJ*, 149, 120, doi: [10.1088/0004-6256/149/4/120](https://doi.org/10.1088/0004-6256/149/4/120)
- Li, K., Xia, Q.-Q., Kim, C.-H., et al. 2021a, *ApJ*, 922, 122, doi: [10.3847/1538-4357/ac242f](https://doi.org/10.3847/1538-4357/ac242f)
- . 2021b, *AJ*, 162, 13, doi: [10.3847/1538-3881/abfc53](https://doi.org/10.3847/1538-3881/abfc53)
- Li, L.-Z., Li, K., Gao, X., et al. 2024a, *MNRAS*, 527, 3982, doi: [10.1093/mnras/stad3251](https://doi.org/10.1093/mnras/stad3251)
- Li, X.-Z., Zhu, Q.-F., Ding, X., et al. 2024b, *ApJS*, 271, 32, doi: [10.3847/1538-4365/ad226a](https://doi.org/10.3847/1538-4365/ad226a)
- Lin, J., Wang, X., Mo, J., et al. 2022, *MNRAS*, 509, 2362, doi: [10.1093/mnras/stab2812](https://doi.org/10.1093/mnras/stab2812)
- . 2023a, *MNRAS*, 523, 2172, doi: [10.1093/mnras/stad994](https://doi.org/10.1093/mnras/stad994)
- Lin, J., Wu, C., Wang, X., et al. 2023b, *Nature Astronomy*, 7, 223, doi: [10.1038/s41550-022-01783-z](https://doi.org/10.1038/s41550-022-01783-z)
- Lin, J., Wu, C., Xiong, H., et al. 2024, *Nature Astronomy*, 8, 491, doi: [10.1038/s41550-023-02188-2](https://doi.org/10.1038/s41550-023-02188-2)
- Lindner, R. R., Vera-Ciro, C., Murray, C. E., et al. 2015, *AJ*, 149, 138, doi: [10.1088/0004-6256/149/4/138](https://doi.org/10.1088/0004-6256/149/4/138)
- Liu, N., Fu, J.-N., Zong, W., et al. 2019, *Research in Astronomy and Astrophysics*, 19, 075, doi: [10.1088/1674-4527/19/5/75](https://doi.org/10.1088/1674-4527/19/5/75)
- Liu, N. P., Qian, S. B., Liao, W. P., Huang, Y., & Yuan, Z. L. 2023a, *AJ*, 165, 259, doi: [10.3847/1538-3881/acd04e](https://doi.org/10.3847/1538-3881/acd04e)
- Liu, X., & Tan, H. 1991, *Ap&SS*, 183, 237
- Liu, X.-Y., Li, K., Michel, R., et al. 2023b, *MNRAS*, 519, 5760, doi: [10.1093/mnras/stad026](https://doi.org/10.1093/mnras/stad026)
- Loeb, A., & Gaudi, B. S. 2003, *ApJL*, 588, L117, doi: [10.1086/375551](https://doi.org/10.1086/375551)
- Lu, W., Hrivnak, B. J., & Rush, B. W. 2007, *AJ*, 133, 255, doi: [10.1086/509604](https://doi.org/10.1086/509604)
- Lucy, L. B. 1967, *ZA*, 65, 89
- . 1968a, *ApJ*, 153, 877, doi: [10.1086/149712](https://doi.org/10.1086/149712)
- . 1968b, *ApJ*, 151, 1123, doi: [10.1086/149510](https://doi.org/10.1086/149510)
- . 1976, *ApJ*, 205, 208, doi: [10.1086/154265](https://doi.org/10.1086/154265)
- Lucy, L. B., & Wilson, R. E. 1979, *ApJ*, 231, 502, doi: [10.1086/157212](https://doi.org/10.1086/157212)
- Luo, A. L., Zhao, Y.-H., Zhao, G., et al. 2015, *Research in Astronomy and Astrophysics*, 15, 1095, doi: [10.1088/1674-4527/15/8/002](https://doi.org/10.1088/1674-4527/15/8/002)
- Marsh, F. M., Prince, T. A., Mahabal, A. A., et al. 2017, *MNRAS*, 465, 4678, doi: [10.1093/mnras/stw2110](https://doi.org/10.1093/mnras/stw2110)
- Masci, F. J., Laher, R. R., Rusholme, B., et al. 2019, *PASP*, 131, 018003, doi: [10.1088/1538-3873/aae8ac](https://doi.org/10.1088/1538-3873/aae8ac)
- Nelson, R. H. 2007, *Information Bulletin on Variable Stars*, 5760, 1
- . 2008, *Information Bulletin on Variable Stars*, 5820, 1
- . 2009a, *Information Bulletin on Variable Stars*, 5875, 1
- . 2009b, *Information Bulletin on Variable Stars*, 5875, 1
- . 2013, *Information Bulletin on Variable Stars*, 6050, 1

- O'Connell, D. J. K. 1951, *Publications of the Riverview College Observatory*, 2, 85
- Pagel, L. 2018, *Information Bulletin on Variable Stars*, 6244, 1, doi: [10.22444/IBVS.6244](https://doi.org/10.22444/IBVS.6244)
- Paki, E., & Poro, A. 2024, arXiv e-prints, arXiv:2405.18618, doi: [10.48550/arXiv.2405.18618](https://doi.org/10.48550/arXiv.2405.18618)
- Panchal, A., & Joshi, Y. C. 2021, *AJ*, 161, 221, doi: [10.3847/1538-3881/abea0c](https://doi.org/10.3847/1538-3881/abea0c)
- Papageorgiou, A., Christopoulou, P.-E., Ferreira Lopes, C. E., et al. 2023, *AJ*, 165, 80, doi: [10.3847/1538-3881/aca65a](https://doi.org/10.3847/1538-3881/aca65a)
- Pavlenko, Y. V., Evans, A., Banerjee, D. P. K., et al. 2018, *A&A*, 615, A120, doi: [10.1051/0004-6361/201832717](https://doi.org/10.1051/0004-6361/201832717)
- Pi, Q.-f., Zhang, L.-y., Bi, S.-l., et al. 2017, *AJ*, 154, 260, doi: [10.3847/1538-3881/aa9438](https://doi.org/10.3847/1538-3881/aa9438)
- Pojmanski, G. 1997, *AcA*, 47, 467, doi: [10.48550/arXiv.astro-ph/9712146](https://doi.org/10.48550/arXiv.astro-ph/9712146)
- . 1998, *AcA*, 48, 35, doi: [10.48550/arXiv.astro-ph/9802330](https://doi.org/10.48550/arXiv.astro-ph/9802330)
- . 2002, *AcA*, 52, 397, doi: [10.48550/arXiv.astro-ph/0210283](https://doi.org/10.48550/arXiv.astro-ph/0210283)
- Pollacco, D. L., Skillen, I., Collier Cameron, A., et al. 2006, *PASP*, 118, 1407, doi: [10.1086/508556](https://doi.org/10.1086/508556)
- Prša, A. 2018, *Modeling and Analysis of Eclipsing Binary Stars; The theory and design principles of PHOEBE*, doi: [10.1088/978-0-7503-1287-5](https://doi.org/10.1088/978-0-7503-1287-5)
- Qian, S. 2001, *MNRAS*, 328, 914, doi: [10.1046/j.1365-8711.2001.04921.x](https://doi.org/10.1046/j.1365-8711.2001.04921.x)
- Qian, S.-B., He, J.-J., Zhang, J., et al. 2017, *Research in Astronomy and Astrophysics*, 17, 087, doi: [10.1088/1674-4527/17/8/87](https://doi.org/10.1088/1674-4527/17/8/87)
- Ricker, G. R., Latham, D. W., Vanderspek, R. K., et al. 2010, in *American Astronomical Society Meeting Abstracts*, Vol. 215, American Astronomical Society Meeting Abstracts #215, 450.06
- Robertson, J. A., & Eggleton, P. P. 1977, *MNRAS*, 179, 359, doi: [10.1093/mnras/179.3.359](https://doi.org/10.1093/mnras/179.3.359)
- Ruciński, S. M. 1969, *AcA*, 19, 245
- Rucinski, S. M., Lu, W., & Mochmacki, S. W. 2000, *AJ*, 120, 1133, doi: [10.1086/301458](https://doi.org/10.1086/301458)
- Shappee, B. J., Prieto, J. L., Grupe, D., et al. 2014, *ApJ*, 788, 48, doi: [10.1088/0004-637X/788/1/48](https://doi.org/10.1088/0004-637X/788/1/48)
- Stassun, K. G., Oelkers, R. J., Pepper, J., et al. 2018, *AJ*, 156, 102, doi: [10.3847/1538-3881/aad050](https://doi.org/10.3847/1538-3881/aad050)
- Stepien, K. 2006, *AcA*, 56, 347, doi: [10.48550/arXiv.astro-ph/0701529](https://doi.org/10.48550/arXiv.astro-ph/0701529)
- Stepień, K. 2011, *AcA*, 61, 139, doi: [10.48550/arXiv.1105.2645](https://doi.org/10.48550/arXiv.1105.2645)
- Sun, W., Chen, X., Deng, L., & de Grijs, R. 2020a, *ApJS*, 247, 50, doi: [10.3847/1538-4365/ab7894](https://doi.org/10.3847/1538-4365/ab7894)
- . 2020b, *ApJS*, 247, 50, doi: [10.3847/1538-4365/ab7894](https://doi.org/10.3847/1538-4365/ab7894)
- van Hamme, W. 1993, *AJ*, 106, 2096, doi: [10.1086/116788](https://doi.org/10.1086/116788)
- Van Hamme, W., & Wilson, R. E. 2007, *ApJ*, 661, 1129, doi: [10.1086/517870](https://doi.org/10.1086/517870)
- Čeki, A., Şenavcı, H. V., Latković, O., et al. 2024, *MNRAS*, 532, 3582, doi: [10.1093/mnras/stae1709](https://doi.org/10.1093/mnras/stae1709)
- Vijaya, A., & Sriram, K. 2023, *Research in Astronomy and Astrophysics*, 23, 055009, doi: [10.1088/1674-4527/acc154](https://doi.org/10.1088/1674-4527/acc154)
- Watson, C. L., Henden, A. A., & Price, A. 2006, *Society for Astronomical Sciences Annual Symposium*, 25, 47
- West, A. A., Weisenburger, K. L., Irwin, J., et al. 2015, *ApJ*, 812, 3, doi: [10.1088/0004-637X/812/1/3](https://doi.org/10.1088/0004-637X/812/1/3)
- West, A. A., Morgan, D. P., Bochanski, J. J., et al. 2011, *AJ*, 141, 97, doi: [10.1088/0004-6256/141/3/97](https://doi.org/10.1088/0004-6256/141/3/97)
- Wilson, R. E. 1979, *ApJ*, 234, 1054, doi: [10.1086/157588](https://doi.org/10.1086/157588)
- . 1990, *ApJ*, 356, 613, doi: [10.1086/168867](https://doi.org/10.1086/168867)
- Wilson, R. E., & Devinney, E. J. 1971, *ApJ*, 166, 605, doi: [10.1086/150986](https://doi.org/10.1086/150986)
- Wilson, R. E., & Van Hamme, W. 2014, *ApJ*, 780, 151, doi: [10.1088/0004-637X/780/2/151](https://doi.org/10.1088/0004-637X/780/2/151)
- Wilson, R. E., Van Hamme, W., & Terrell, D. 2010, *ApJ*, 723, 1469, doi: [10.1088/0004-637X/723/2/1469](https://doi.org/10.1088/0004-637X/723/2/1469)
- Wu, J.-F., Zhu, L.-Y., Matekov, A., et al. 2024, *MNRAS*, 529, 3113, doi: [10.1093/mnras/stae590](https://doi.org/10.1093/mnras/stae590)
- Xiong, J., Ding, X., Li, J., et al. 2024, *ApJS*, 270, 20, doi: [10.3847/1538-4365/ad0ceb](https://doi.org/10.3847/1538-4365/ad0ceb)
- Yakut, K., & Eggleton, P. P. 2005, *ApJ*, 629, 1055, doi: [10.1086/431300](https://doi.org/10.1086/431300)
- Yang, Y., Michel, R., Yuan, H., Wang, S., & Tamayo, F. 2023, *MNRAS*, 522, 3076, doi: [10.1093/mnras/stad1141](https://doi.org/10.1093/mnras/stad1141)
- Yang, Y.-G. 2011, *Research in Astronomy and Astrophysics*, 11, 181, doi: [10.1088/1674-4527/11/2/006](https://doi.org/10.1088/1674-4527/11/2/006)
- Yang, Y. G., Qian, S. B., Zhang, L. Y., Dai, H. F., & Soonthornthum, B. 2013, *AJ*, 146, 35, doi: [10.1088/0004-6256/146/2/35](https://doi.org/10.1088/0004-6256/146/2/35)
- Yıldız, M. 2014, *MNRAS*, 437, 185, doi: [10.1093/mnras/stt1874](https://doi.org/10.1093/mnras/stt1874)
- Yildiz, M., & Doğan, T. 2013, *MNRAS*, 430, 2029, doi: [10.1093/mnras/stt028](https://doi.org/10.1093/mnras/stt028)
- Zhang, B., Liu, C., & Deng, L.-C. 2020a, *ApJS*, 246, 9, doi: [10.3847/1538-4365/ab55ef](https://doi.org/10.3847/1538-4365/ab55ef)
- Zhang, B., Li, J., Yang, F., et al. 2021, *ApJS*, 256, 14, doi: [10.3847/1538-4365/ac0834](https://doi.org/10.3847/1538-4365/ac0834)
- Zhang, J.-C., Wang, X.-F., Mo, J., et al. 2020b, *PASP*, 132, 125001, doi: [10.1088/1538-3873/abbea2](https://doi.org/10.1088/1538-3873/abbea2)
- Zhao, G., Zhao, Y.-H., Chu, Y.-Q., Jing, Y.-P., & Deng, L.-C. 2012, *Research in Astronomy and Astrophysics*, 12, 723, doi: [10.1088/1674-4527/12/7/002](https://doi.org/10.1088/1674-4527/12/7/002)
- Zucker, S., Mazeh, T., & Alexander, T. 2007, *ApJ*, 670, 1326, doi: [10.1086/521389](https://doi.org/10.1086/521389)